Neural circuits in the mouse retina support color vision in the upper visual field

Klaudia P. Szatko[1-3*], Maria M. Korympidou[1,3,4*], Yanli Ran[1,4], Philipp Berens[1,2,5], Deniz Dalkara[6], Timm Schubert[1,4], Thomas Euler[1,2,4], Katrin Franke[1,2,#]

[1]Institute for Ophthalmic Research, University of Tübingen, Germany

[2]Bernstein Center for Computational Neuroscience, University of Tübingen, Germany

[3]Graduate Training Center of Neuroscience, International Max Planck Research School, University of Tübingen, Germany

[4]Center for Integrative Neuroscience, University of Tübingen, Germany

[5]Institute for Bioinformatics and Medical Informatics, University of Tübingen, Germany

[6]Sorbonne Université, INSERM, CNRS, Institut de la Vision, Paris, France

*These authors contributed equally to this work

[#]Correspondence at katrin.franke@cin.uni-tuebingen.de

ABSTRACT

Color vision is essential to the survival of most animals. Its neural basis lies in the retina, where chromatic signals from different photoreceptor types sensitive to distinct wavelengths are locally compared by neural circuits. Mice, like most mammals, are generally dichromatic and have two cone photoreceptor types. However, in the ventral retina most cones display the same spectral preference, impairing spectral comparisons necessary for color vision. This conflicts with behavioral evidence showing that mice can discriminate colors only in the corresponding upper visual field. Here, we systematically investigated the neural circuits underlying mouse color vision across three processing stages of the retina by recording the output of cones, bipolar and ganglion cells using two-photon imaging. Surprisingly, we found that across all retinal layers most color-opponent cells were located in the ventral retina. This started at the level of the cone output, where color-opponency was mediated by horizontal cells and likely involving rod photoreceptors. Next, bipolar cells relayed the chromatic information to ganglion cells in the inner retina, where type-specific, non-linear center-surround interactions resulted in specific color-opponent output channels to the brain. This suggests that neural circuits in the mouse retina are specifically tuned to extract color information from the upper visual field, aiding robust detection of aerial predators and ensuring the animal's survival.

INTRODUCTION

Color vision is key to guiding behavior in animals (reviewed in (Gerl and Morris, 2008)), including navigating in ecological niches (e.g. (Pfeiffer and Homberg, 2007)), communicating with conspecifics (e.g. (Huang et al., 2014)), foraging as well as detecting predators and prey (e.g. (Dominy and Lucas, 2001; Potier et al., 2018)). In the retina, signals from different photoreceptor types sensitive to different wavelengths are locally compared by downstream retinal circuits to extract chromatic information present in the visual input (reviewed in (Thoreson and Dacey, 2019)). These circuits have been studied in detail in trichromatic primates (reviewed in (Dacey, 2000; Neitz and Neitz, 2011; Thoreson and Dacey, 2019)). Here, signals from short (S; “blue”), medium (M; “green”) and long (L; “red”) wavelength-sensitive cone photoreceptors are processed via two main opponent pathways: red-green (L vs. M) and blue-yellow opponency (S vs. L+M). While the former is mainly based on random and cone type-unselective wiring of the high-acuity midget system (Martin et al., 2001; Buzás et al., 2006; Field et al., 2010; Crook et al., 2011; Wool et al., 2019), blue-yellow opponency relies on precise connectivity in cone type-selective retinal circuits (Dacey and Lee, 1994; Calkins et al., 1998; Crook et al., 2009a).

Compared to primates, the retinal circuits underlying dichromatic vision in other mammals are far from being understood (reviewed in (Puller and Haverkamp, 2011; Marshak and Mills, 2014)). This is also true for the mouse – despite its prominent role as one of today’s most frequently used model in visual neuroscience. Mice express S- and M-opsin (Szél et al., 1992) most sensitive to UV and green light, respectively (Fig. 1a) (Jacobs et al., 1991; Baden et al., 2013). In addition, M-cones co-express S-opsin, with co-expression increasing towards the ventral retina (Fig. 1b) (Röhlich et al., 1994; Applebury et al., 2000). In contrast, S-cones exclusively expressing S-opsin (“true” S-cones) make up ~5% of all cones and are homogeneously distributed across the retina (Haverkamp et al., 2005). This asymmetric opsin distribution results in a mainly green-sensitive dorsal and a UV-sensitive ventral retina (Calderone and Jacobs, 1995; Baden et al., 2013). Nonetheless, behavioral studies have demonstrated that mice can discriminate between light spots of different colors (Jacobs et al., 2004), at least in the upper visual field (Denman et al., 2018). However, the retinal circuits underlying this behavior are largely unknown.

Several neuronal circuits for S vs. M color-opponency have been previously proposed in the mouse retina. Some of these circuits involve wiring with S-cone-selective type 9 bipolar cells (BCs) (Stabio et al., 2018). Others do not require cone type-selective connectivity: For example, alpha retinal ganglion cells (RGCs) located along the horizontal midline exhibit color-opponent responses due to chromatically distinct input to their center and surround (Chang et al., 2013). In addition, rod photoreceptors, whose spectral sensitivity closely matches that of M-cones, may also be involved in color-opponency: They provide an antagonistic surround to JAM-B RGCs located in the S-opsin dominated ventral retina by lateral feedback from horizontal cells (HCs) (Joesch and Meister, 2016). Such a rod-cone opponent mechanism may support color discrimination in the ventral retina despite the lack of substantial M-opsin expression. While all these studies point at the existence of color-opponent signals downstream from mouse photoreceptors, a comprehensive survey of chromatic processing and the retinal circuits underlying mouse color vision (Jacobs et al., 2004; Denman et al., 2018) is still missing.

Therefore, we systematically investigated the basis for color vision in the mouse retina across three consecutive processing stages. We recorded the output signals of cones, BCs and RGCs to chromatic visual stimulation in the *ex-vivo*, whole-mounted retina using two-photon calcium and glutamate imaging. Surprisingly, we found that across all processing layers, color-opponency was largely confined to the S-opsin dominated ventral retina. Here, color-opponent responses were already present at the level of the cone output, mediated by input from HCs and likely involving rod photoreceptors. We further show how BCs forward the chromatic signals from photoreceptors to the inner retina, where different RGC types integrate information from their center and surround in a type specific way, thereby increasing the diversity of chromatic signals available to the brain.

RESULTS

Recording chromatic cone responses in the whole-mounted mouse retina

To characterize chromatic signaling in cones, we recorded synaptic glutamate release from their axon terminals. To this end, we expressed the glutamate biosensor iGluSnFR (Marvin et al., 2013) ubiquitously in the retina using a viral approach (Fig. 1c) (Franke et al., 2017). In the outer plexiform layer (OPL), where the cone axon terminals are located, this approach resulted in iGluSnFR being predominantly expressed in HC processes (Chapot et al., 2017), which are postsynaptic to the photoreceptors. To identify functional release units, we defined regions of interest (ROIs) using a correlation-based approach (Fig. 1d,i; Methods). These functionally defined ROIs formed a regular mosaic within individual scan fields (Suppl. Fig. S1a-h), reminiscent to the mosaic of EM-reconstructed cone axon terminals (Wässle and Riemann, 1978; Behrens et al., 2016). In addition, the ROIs co-localized with anatomical cone axon terminals visualized using Sulforhodamine-101 (SR-101; Suppl. Fig. S1i) (Chapot et al., 2017). Together, this suggests that our ROIs correspond to individual cone axon terminals and that densely packed rod photoreceptors – the only other source of glutamate release in the outer retina – do not contribute detectably to the glutamate signals recorded in the OPL (Discussion). For simplicity, we will in the following refer to ROIs in OPL scan fields as cones.

In total, we recorded light-evoked glutamate responses from 2,945 cones (n=52 scan fields, n=9 mice) located in dorsal and ventral retina using full-field (700 µm in diameter) as well as center (150 µm in diameter) and surround (annulus; full-field – center) green and UV light flashes (Fig. 1e,g; Methods). For each cone that passed our quality criterion (Methods), we quantified the chromatic preference of full-field, center and surround responses by estimating the spectral contrast (*SC*; for UV- and green-sensitivity $SC<0$ and $SC>0$, respectively). For sufficient center stimulation of all cones within one scan field, the size of the center stimulus was slightly larger than the size of the scan field and, hence, did not relate to the anatomical size of cones.

Ventral cone photoreceptors display color-opponent responses

We found that the chromatic preference of cone full-field and center responses largely matched the opsin expression across the mouse retina. Generally, as vertebrate cones are Off cells and hyperpolarize upon an increase in light, cone center and full-field responses were characterized by a decrease in glutamate release (Fig. 1e,g). In agreement with the predominance of M-opsin in the dorsal retina, the majority of dorsal cones displayed a strong response to green full-field and center flashes (Figs. 1e-h, 2a,b; SC_{center}=0.38±0.44, $SC_{full\text{-}field}$=0.37±0.45). Due to the long sensitivity tail of M-opsin to shorter wavelengths (cf. Fig. 1a), most dorsal cones showed a small additional response to UV. In addition, consistent with the homogeneous distribution of S-cones (Haverkamp et al., 2005), a small number of dorsal cones responded strongly to UV light (see e.g. cone (2) in Fig. 1e-h). Ventral cones exhibited UV-dominant responses to full-field and center flashes (Figs. 1j-m, 2a,b; SC_{center}=-0.7±0.43, $SC_{full\text{-}field}$=-1.12±0.43), as expected from the co-expression of S-opsin in ventral M-cones (e.g. (Applebury et al., 2000)).

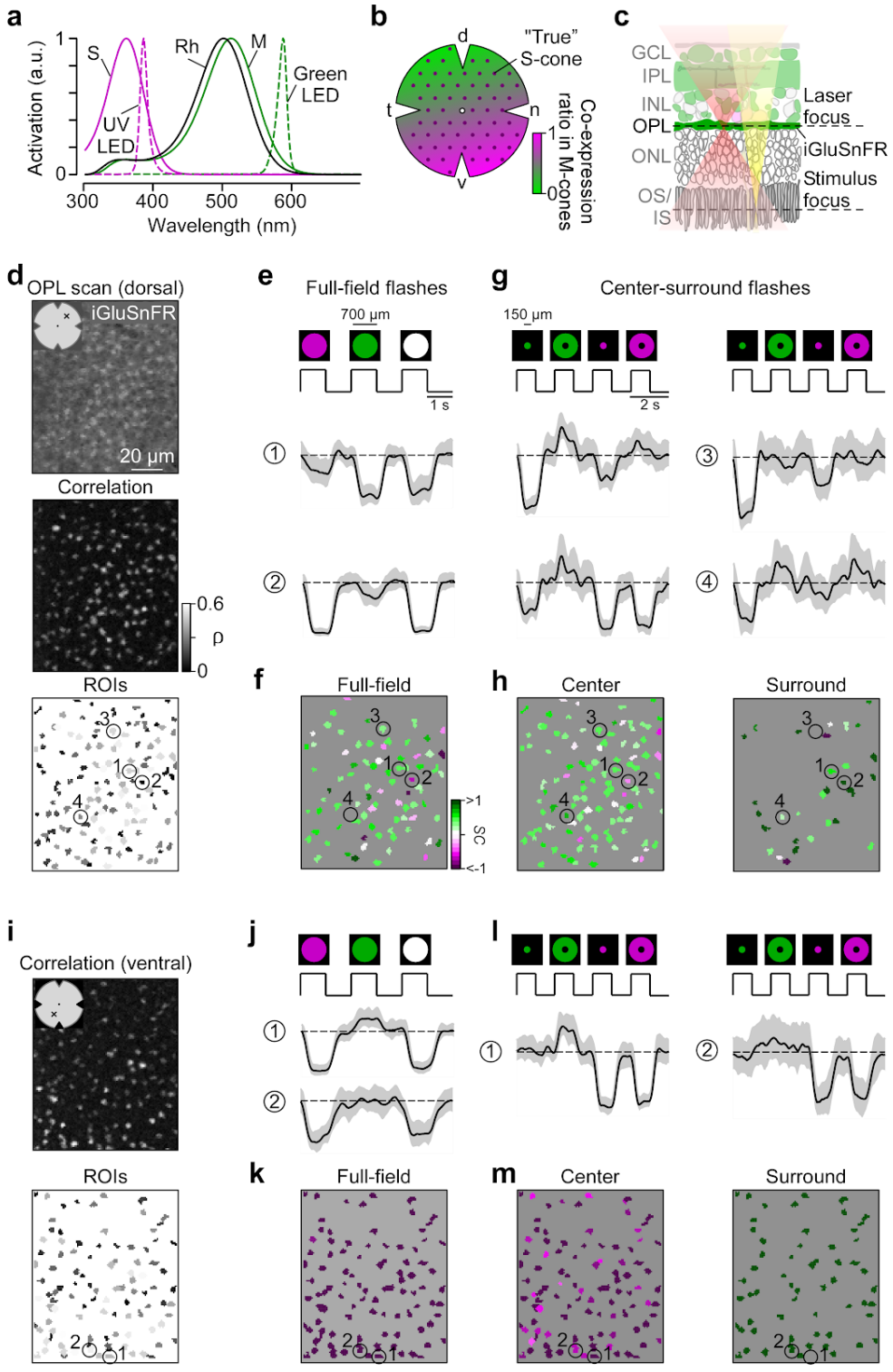

Figure 1 | Imaging chromatic signals from cone axon terminals in the whole-mounted mouse retina. a, Sensitivity spectra of mouse S- (magenta) and M-opsin (green) and rhodopsin (black; Rh), with emission spectra of UV (magenta, dotted) and green LED (green, dotted) used in the visual stimulator. **b,** Schematic illustrating the distribution of cone photoreceptors across the mouse retina. Dots and shading represent distribution of "true" S-cones and co-expression ratio of S- and M-opsin in mouse M-cones, respectively. d: dorsal; n: nasal; v: ventral; t: temporal. **c,** Schematic illustrating the experimental setup for cone recordings. OS/IS: outer/inner segment; ONL: outer nuclear layer; OPL: outer plexiform layer; INL: inner nuclear layer; IPL: inner plexiform layer; GCL: ganglion cell layer. Red and yellow shading illustrate laser and stimulus beam, respectively. **d,** Example scan field (93x110 µm, 3.9 Hz) located in the dorsal retina, showing iGluSnFR expression in the OPL (top), correlation image (middle) and respective ROI mask (bottom). For display, the light artifact on the left side of scan fields was cut, resulting in 108x128 pixels (instead of 128x128). **e,** Cone responses of exemplary ROIs from (d, bottom) to

full-field UV, green and white flashes. As vertebrate photoreceptors are Off cells, light responses correspond to a decrease in glutamate release. Traces show mean glutamate release with s.d. shading. Dotted line indicates baseline. **f,** Cells from (d, bottom) color-coded according to their *SC* in response to full-field flashes. **g,** Glutamate traces of cells from (d, bottom) in response to UV and green center and surround flashes. **h,** Cells from (d, bottom) color-coded based on center (left) and surround *SC* (right). **i,** Correlation image (top) and ROI mask (bottom) for an exemplary scan field located in the ventral retina. **j-m,** Like (e-h), but for cells shown in (i, bottom).

In contrast to full-field and center responses, the chromatic preference of cone surround responses did not strictly follow the opsin distribution across the retina. We focused on antagonistic responses where center and surround stimuli result in decrease and increase in glutamate release, respectively. We found that many dorsal cones showed a stronger increase in glutamate to green than to UV surround stimulation (Figs. 1g,h, 2c; $SC_{surround}$=0.39±1.02; n=216/671), matching the spectral preference of center and full-field responses. Most ventral cones showed an increase in glutamate solely to green surround stimuli (Figs. 1l,m, 2c; $SC_{surround}$=1.2±0.42; n=841/1,337), contrasting their UV preference for center and full-field responses. This resulted in color-opponent center-surround RFs and color-opponent full-field responses (Figs. 1j,k, 2a; $SC_{full\text{-}field}$<-1; n=937/1,329). Surprisingly, UV-sensitive cones in ventral and dorsal scan fields consistently showed the same response polarity for both UV center and surround stimulation (see e.g. cones (1) and (2) in Fig. 1l), which might be due to increased scattering of UV light (Discussion).

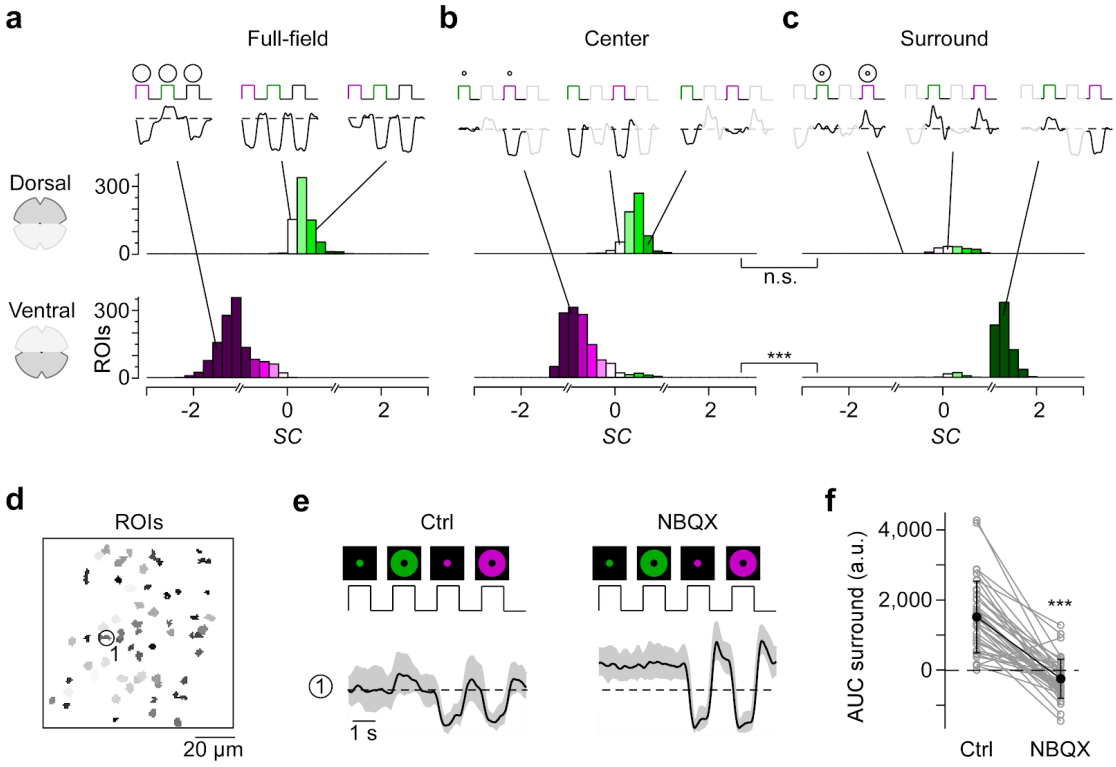

Figure 2 | Differential chromatic processing in ventral and dorsal cones. a-c, Distribution of spectral contrast (*SC*) of dorsal (top) and ventral (bottom) cones in response to full-field (a), center (b) and surround (c) flashes. Mean glutamate traces of single cones above histograms illustrate the diversity of cone responses to chromatic stimuli. Interestingly, only a fraction of cones showed antagonistic surround responses characterized by an increase in glutamate release (Discussion). Breaks in the x axis indicate where different equations for estimating *SC* were used (Methods). n.s.: not significant (p>0.05); ***: p<0.001; linear mixed-effects model for partially paired data (for details, see Methods and Suppl. Information). **d,** ROI mask of scan field located in ventral retina. **e,** Glutamate traces of exemplary cone from (d) in response to UV and green center and surround flashes under control and drug condition (50 µM NBQX). Traces show mean glutamate release with s.d. shading. **f,** Effect of

bath-applied NBQX on area under the curve (AUC) of green-sensitive surround responses of ventral cones (n=40 ROIs, n=3 scan fields, n=2 mice). ***: p<0.001; Wilcoxon signed-rank test.

Next, we investigated the origin of the green surround responses in the ventral retina. As S-opsin expression strongly increases towards the ventral retina, the main source of green sensitivity should be rod photoreceptors (*cf.* Fig. 1a). Recently, it has been proposed that rod signals are relayed to cones via HCs (Joesch and Meister, 2016). To test this hypothesis, we recorded cone responses to chromatic center-surround stimuli while blocking light-evoked HC feedback using NBQX, an antagonist of AMPA/kainate-type glutamate receptors (Fig. 2d,e; see e.g. (Chapot et al., 2017)). This caused a significant decrease in green-sensitive surround responses in ventral cones (Fig. 2f), confirming that HCs contribute to generating color-opponent responses in cones.

In summary, we found that the chromatic preference of a cone's center and full-field response mirrored the overall opsin distribution at the recording site, with largely UV- and green-sensitive responses in the ventral and dorsal retina, respectively. However, while in dorsal cones the chromatic preference of center and surround was very similar, ventral cones systematically exhibited a strong green-shift in the chromatic preference of their antagonistic surround, likely involving HC input driven by rods. This results in color-opponent responses in most ventral cones, demonstrating that color-opponency is already present at the first synapse of the mouse visual system.

Bipolar cells relay color-opponent responses of cones to the inner retina

Next, we investigated how the chromatic information present in the cone output is relayed to the inner retina by the BC population. In the mouse retina, the signals from photoreceptors are distributed among 14 BC types (Behrens et al., 2016; Shekhar et al., 2016; Franke et al., 2017), with their axonal arbors stratifying at different levels of the inner plexiform layer (IPL) (Helmstaedter et al., 2013; Kim et al., 2014; Greene et al., 2016).

To record responses from BCs, we again used ubiquitous expression of iGluSnFR. In contrast to previous work (Franke et al., 2017), where the scan fields were parallel to the retinal layers, we here employed axial scanning using an electrically tunable lens to rapidly shift the focal plane of the excitation laser (Zhao et al., 2019). This allowed us to simultaneously record the glutamatergic signals across the entire IPL (Fig. 3a). Like before, we defined ROIs based on local image correlation (Fig. 3b; Methods) (Zhao et al., 2019). To register the IPL depth of each ROI, we used the two characteristic dendritic plexi of cholinergic starburst amacrine cells as landmarks (*cf.* Fig. 1b in (Franke et al., 2017)); these "ChAT bands" were visible through their TdTomato-expression in our transgenic animals.

In total, we recorded light-evoked BC glutamate release from 3,604 ROIs (n=21 scan fields, n=5 mice) across the entire IPL (Suppl. Fig. S2a). As expected from the type-specific axonal stratification profiles of BCs (Helmstaedter et al., 2013; Kim et al., 2014; Greene et al., 2016), ROIs located at different IPL depths showed distinct responses to the local chirp stimulus (Fig. 3c; 100 µm in diameter). To investigate chromatic signaling in BCs, we used a 10 Hz center-surround UV and green flicker stimulus (Fig. 3d; Methods). From the glutamate responses of each ROI, we estimated the preferred stimulus ("event-triggered stimulus kernels") for the four conditions – center and surround for both UV and green – to obtain the BC ROI's chromatic RF preferences (as *SC*, see above). In addition, we computed the mean glutamate event of each ROI to a full-field UV and green light spot ("stimulus-triggered event

kernels") to test for full-field color-opponency (quantified by the linear correlation coefficient (ρ) between UV and green event kernels; Methods).

In line with the chromatic preference of cone center responses (*cf.* Fig. 2), we found that BCs located in the ventral and dorsal retina showed a UV- and green-dominant center, respectively (Figs. 3d-h, 4a,b; ventral: SC_{center}=-0.44±0.24, dorsal: SC_{center}=0.1±0.22). Overall, we did not observe large differences in *SC* of BC center responses across the IPL (Suppl. Fig. S2b). This is consistent with recent connectomic data demonstrating that, except for type 9 and type 1 BC (Discussion), mouse BCs indiscriminately contact all cone types within their dendritic tree (Behrens et al., 2016).

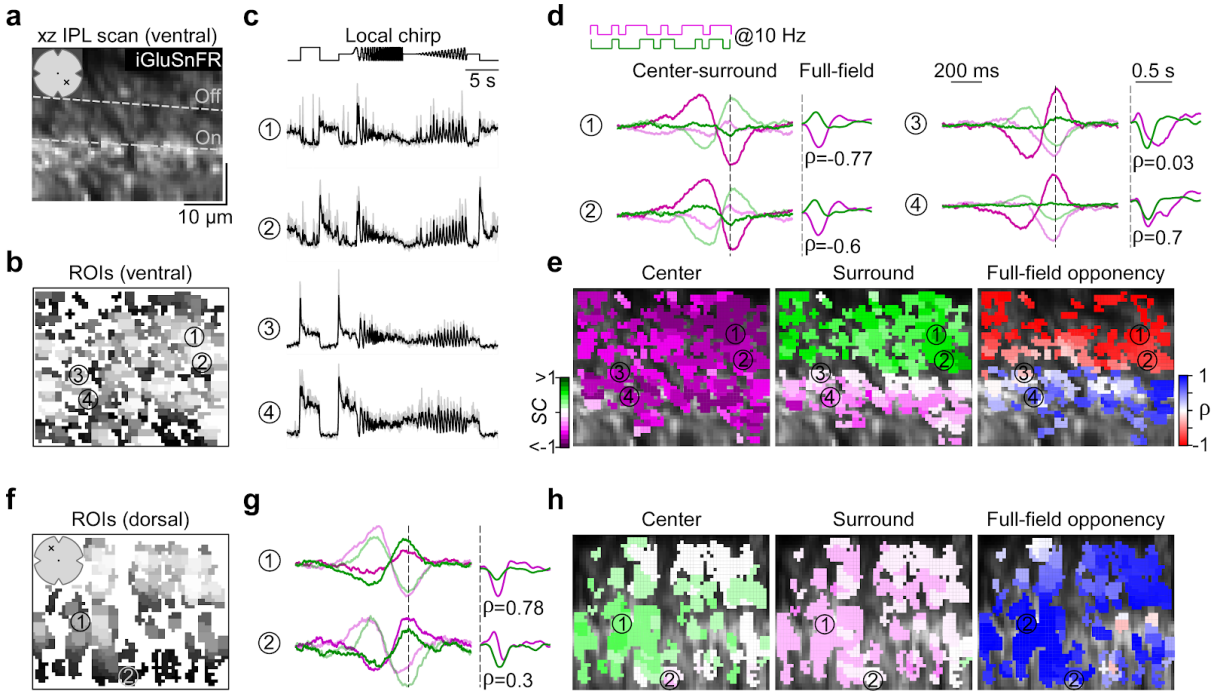

Figure 3 | Recording chromatic bipolar cell responses across the inner plexiform layer. a, Vertical (xz) scan field (48x50 µm, 11.17 Hz) located in the ventral retina showing iGluSnFR expression across the inner plexiform layer (IPL). Dotted lines indicate On and Off ChAT band, respectively. **b,** ROI mask for scan field shown in (a). For details on ROI detection, see Methods. **c,** Mean glutamate traces (black, s.d. shading in grey; n=5 trials) of ROIs indicated in (b) in response to a local chirp stimulus. **d,** Temporal center (bright) and surround (dim) kernels (event-triggered average) estimated from a 10 Hz center-surround flicker stimulus of UV and green LED (left) and mean glutamate events (stimulus-triggered event) in response to a full-field UV and green stimulus (right) for ROIs indicated in (b). Linear correlation coefficient (ρ) of mean glutamate events indicated below traces. Dotted lines indicate time point of response/stimulus. **e,** ROI mask from (b) color-coded according to center (left) and surround spectral contrast (*SC*) (middle) as well as correlation (right). **f,** ROI mask of a scan field located in the dorsal retina. **g,h,** Like (d,e), but for dorsal scan field shown in (f).

The chromatic preference of BC surround responses differed from that of their respective center responses, particularly in the ventral retina. Surround responses in ventral BCs were systematically shifted towards green ($SC_{surround}$=0.21±0.27), resulting in color-opponent full-field responses (ρ<-0.3) for approx. half of all ventral BC ROIs (Figs. 3d,e, 4a-d; n=762/1,714). Notably, the difference in *SC* of center and surround (SC_{Diff}) as well as the fraction of color-opponent responses was significantly larger for ROIs located in the IPL's Off sublamina compared to those in the On sublamina (Figs. 4e,f, S2c; Discussion). Dorsal BCs showed a shift towards slightly higher UV-sensitivity in their surround responses (Figs. 3g,h, 4a,b; $SC_{surround}$=0.03±0.19), which was stronger for On compared to Off BCs (Fig. 4e) but much smaller than for ventral BCs; therefore only very few (n=64/1,474) dorsal BCs showed

color-opponent full-field responses (Fig. 4f). In addition, we obtained comparable results when modulating green and UV sinusoidally (Suppl. Fig. S3) – a visual stimulus often used in retinal studies on chromatic processing (e.g. (Dacey and Lee, 1994; Chang et al., 2013)).

In summary, our data show that BCs provide chromatically tuned excitatory drive to downstream amacrine cell (AC) and RGC circuits. Furthermore, the difference between On and Off BCs indicates that they might not simply relay the chromatic information from cones to the inner retina.

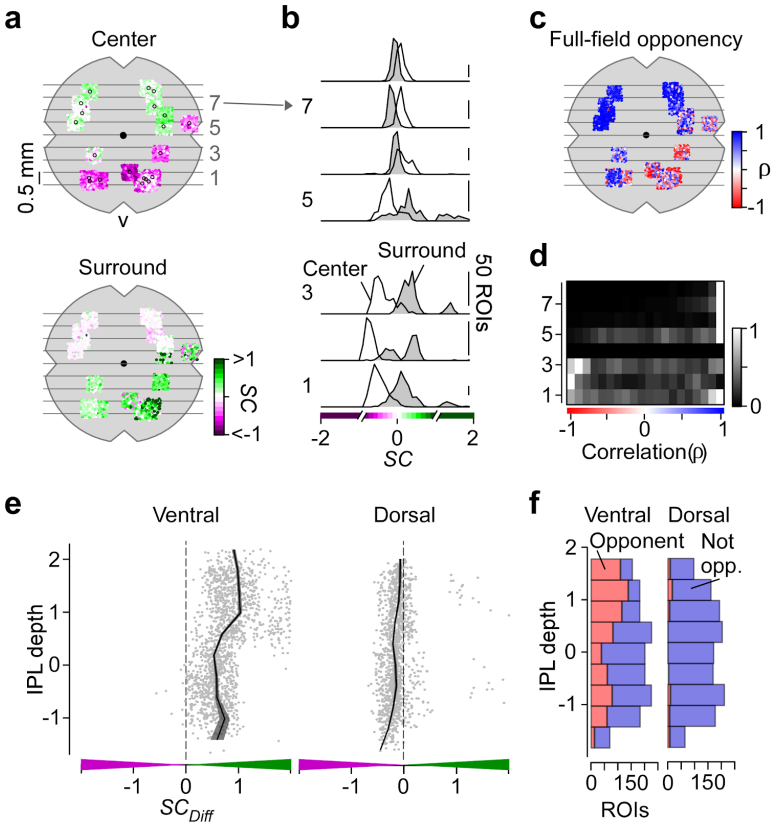

Figure 4 | Chromatic signals of bipolar cells match cone responses across the retina. a, Distribution of recorded inner plexiform layer (IPL) scan fields (black circles), with ROIs color-coded according to their center (top) and surround spectral contrast (*SC*; bottom). ROIs are scattered around scan field center by ± 300 µm in x and y. Grey lines and numbers on the left indicate bins used for analysis in (b) and (d). Bin size: 0.5 mm. **b,** Distribution of center (no fill) and surround (grey fill) *SC* values from ventral to dorsal retina. Numbers indicate bins shown in (a). For all bins, center *SC* was significantly different from surround *SC* (Linear mixed-effects model for partially paired data; see Methods and Suppl. Information). **c,** Same as (a), but color-coded according to correlation coefficient (ρ) of full-field events. **d,** Peak-normalized histograms showing distribution of correlation coefficients from ventral to dorsal retina. Numbers indicate bins shown in (a). Bin size: 0.5 mm. **e,** Difference of center and surround *SC* (SC_{Diff}) across the IPL for ROIs located in the ventral (left) and dorsal (right) retina. SC_{Diff} significantly varied with IPL depth for both ventral and dorsal retina (Generalized additive model; see Methods and Suppl. Information). **f,** Distribution of full-field opponent (red; ρ<-0.3) and non-opponent (blue) ROIs across the IPL for ventral and dorsal scan fields. Number of opponent ROIs significantly varied with IPL depth for ventral and dorsal retina (Generalized additive model; see Methods and Suppl. Information).

Color-opponent responses are preserved at the level of the retinal output

Finally, we investigated how the chromatic information is represented in the population of RGCs. We used the synthetic calcium indicator Oregon Green BAPTA-1 (OGB-1) and bulk-electroporation to uniformly label the ganglion cell layer (GCL; Fig. 5a) (Briggman and Euler, 2011; Baden et al., 2016). This allowed us to densely record somatic signals from

RGCs and displaced ACs (dAC), which make up the mouse GCL at a ratio of roughly 1:1 (Schlamp et al., 2013). We recorded GCL scan fields at different positions along the retina's dorso-ventral axis (*cf.* Fig. 6a). To assign the recorded cells (n=8,429 cells, n=100 scan fields, n=20 mice) to functional RGC and dAC groups (presumably corresponding to single types) previously described (Baden et al., 2016), we presented two achromatic stimuli (full-field chirp and moving bar; Fig. 5b). Like for the BC recordings, we characterized the cells' chromatic preference and full-field opponency by estimating center-surround stimulus and full-field event kernels, respectively, from calcium responses to a 5 Hz center-surround UV and green flicker stimulus (center: 250 µm in diameter) (Fig. 5c).

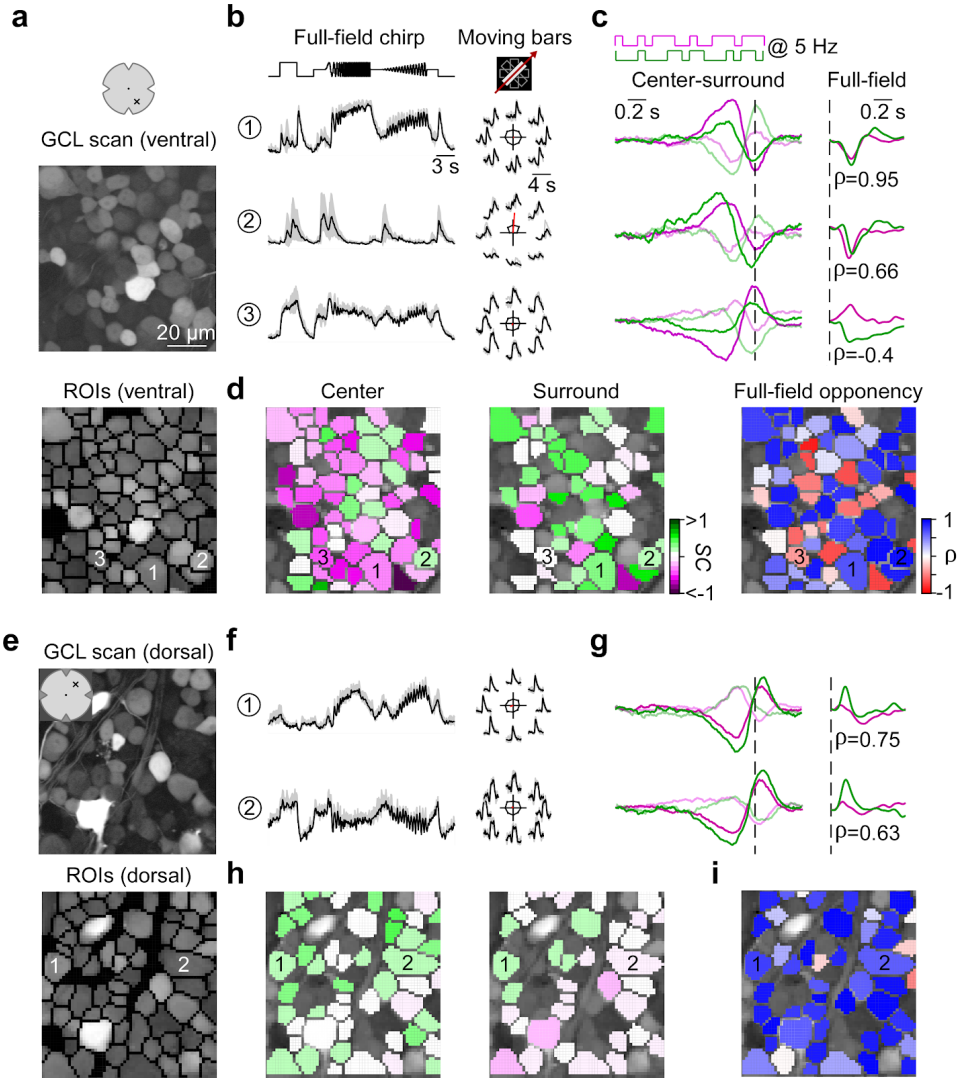

Fig. 5 | Chromatic responses in the ganglion cell layer of the mouse retina. a, Ganglion cell layer (GCL) scan field (top; 95x95 µm, 7.8125 Hz) located in the ventral retina electroporated with the synthetic calcium indicator Oregon Green BAPTA-1 (OGB-1) and corresponding ROI mask (bottom). **b,** Mean calcium traces (black, s.d. shading in grey; n=5 trials) of ROIs indicated in (a, bottom) in response to full-field chirp (left) and moving bars (right). **c,** Temporal center (bright) and surround (dim) kernels estimated from a 5 Hz center-surround flicker stimulus of UV and green LED (left) and mean calcium events in response to a full-field UV and green stimulus (right) for ROIs indicated in (a, bottom). Linear correlation coefficient of full-field events indicated below traces. Dotted lines indicate time point of response/stimulus. **d,** ROIs from (a, bottom) color-coded according to center (left) and surround spectral contrast (*SC*; middle) as well as correlation (right). **e,** Scan field and corresponding ROI mask located in the dorsal retina. **f-i,** Like (b-d), but for scan field shown in (e).

We found that the chromatic preference of GCL cell center responses largely matched the opsin expression, with a gradient of UV- to green-dominated responses from ventral to dorsal retina (Figs. 5d,h, 6a,b; ventral: SC_{center}=-0.35±0.27, dorsal: SC_{center}=0.06±0.25). Notably, the chromatic tuning of center responses was more diverse in the GCL compared to the IPL (Suppl. Fig. S4). For example, we frequently observed ventral GCL cells responding stronger to green than to UV center stimulation (Fig. 5c,d), which was not the case for ventral OPL and IPL recordings.

Surround responses of ventral GCL cells were systematically shifted towards green (Figs. 5c,d, 6a,b; $SC_{surround}$=0.21±0.82), resulting in a large difference in center vs. surround chromatic preference and, thus, in color-opponent full-field responses (n=459/3,418). For dorsal scan fields, the difference between center and surround chromatic preference and, likewise, the fraction of color-opponent responses was smaller ($SC_{surround}$=0.17±0.62; n=80/1,371). Interestingly, in our dataset we only rarely observed GCL cells with center-opponent responses (Suppl. Fig. S5; Discussion), which have been found in primates (e.g. (Crook et al., 2009b)) and some dichromatic mammals (e.g. (Sher and DeVries, 2012)).

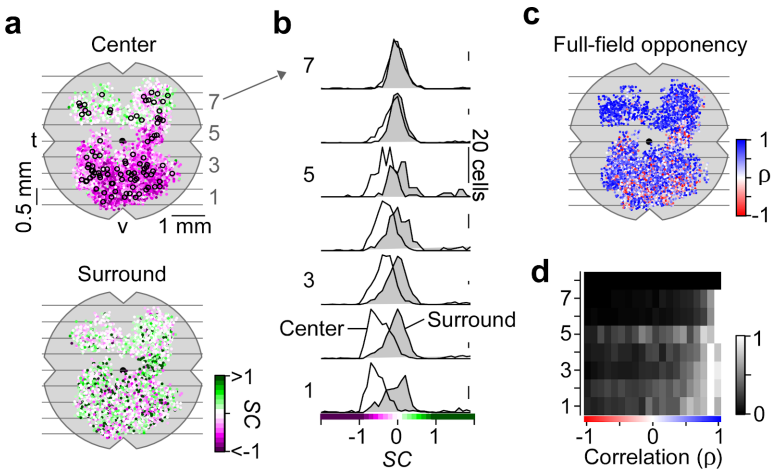

Fig. 6 | Color-opponency at the level of the mouse retinal output. a, Distribution of recorded ganglion cell layer (GCL) scan fields (black circles), with ROIs color-coded according to their center (top) and surround spectral contrast (*SC*; bottom). ROIs are scattered around scan field center by +-300 µm in x and y. Grey lines and numbers on the left indicate bins used for analysis in (b) and (d). Bin size: 0.5 mm. **b,** Distribution of center (no fill) and surround (grey fill) *SC* values from ventral to dorsal retina. Numbers indicate bins shown in (a). For all bins, center *SC* was significantly different from surround *SC* (Linear mixed-effects model for partially paired data; see Methods and Suppl. Information). **c,** Same as (a), but color-coded according to correlation of full-field events (ρ). **d,** Peak-normalized histograms showing distribution of correlation coefficient from ventral to dorsal retina. Numbers indicate bins shown in (a). Bin size: 0.5 mm.

In summary, while color-opponency was largely preserved at the level of the retina´s output layer, our findings suggest that the complexity of chromatic signals increases from the IPL to the GCL. Next, we investigated whether the color-opponent GCL cells correspond to RGCs and/or dACs and if chromatic information is processed in a type-specific manner.

Cell-type specific chromatic processing in mouse retinal ganglion cells

We next allocated the recorded cells to the previously described functional RGC and dAC groups (Baden et al., 2016) based on their responses to the achromatic stimuli (Methods). Because color-opponency was pronounced in the ventral retina, we focused the analysis on ventral scan fields. We found that color-opponent GCL cells were assigned to both RGC and

dAC groups (Fig. 7a, Suppl. Fig. S6), suggesting that color-opponency is a feature of both cell classes. To verify this, we dye-injected and morphologically reconstructed color-opponent GCL cells (n=19) subsequent to functional imaging (Fig. 7b, Suppl. Fig. S7). Consistent with the abundance of color-opponent responses in the GCL (*cf.* Fig. 5c), we found a large variety of dendritic morphologies in our sample, with approx. half (n=8) of the reconstructed cells corresponding to dACs, as identified by the absence of an axon. Due to similar response profiles, 5/19 morphologically identified RGCs and dACs were assigned to the wrong class (Suppl. Fig. S7). Because we were interested in chromatic retinal output, in the following we focused on RGCs (for dACs, see Suppl. Fig. S6).

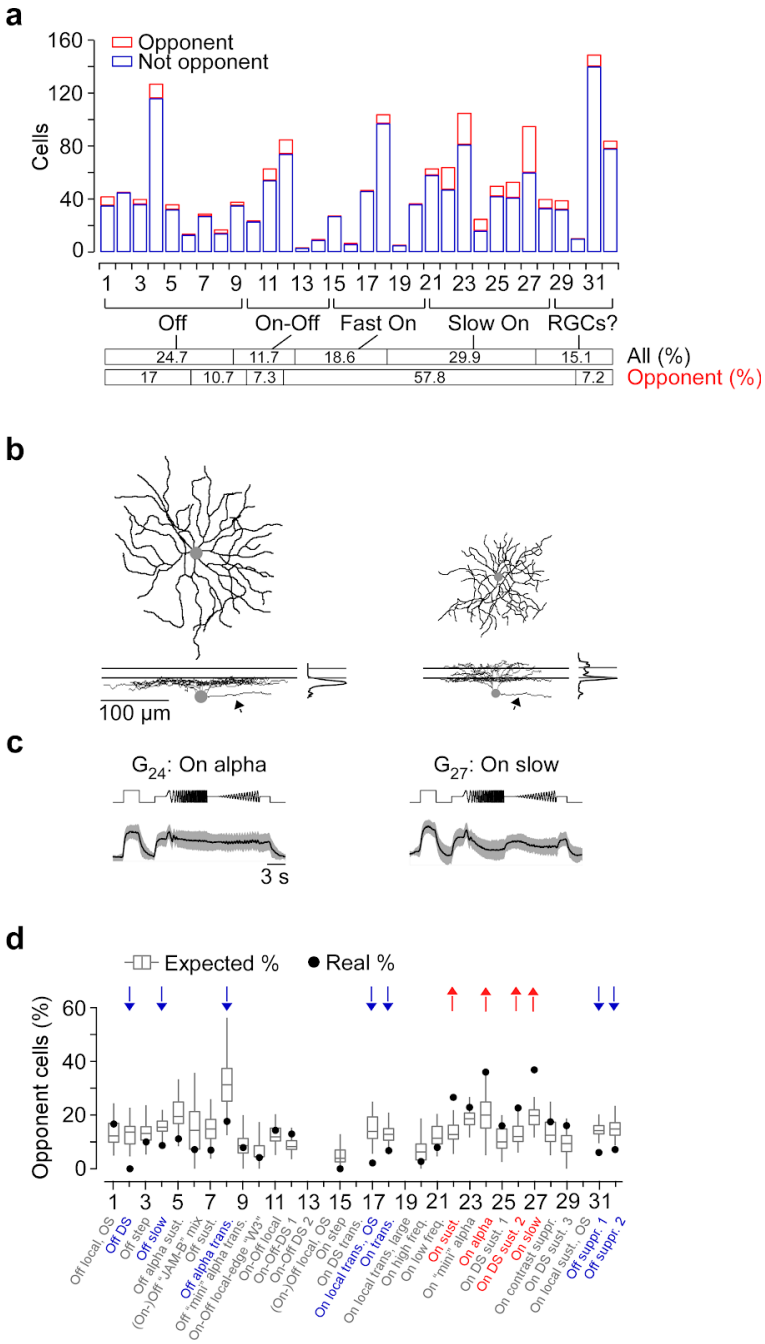

Fig. 7 | The color-opponent output channels of the mouse retina. a, Distribution of ventral color-opponent (red) and non-opponent (blue) RGCs located in the ventral retina. For analysis in (d), only groups with n>10 cells were used. **b,** Dendritic morphologies with stratification profiles of two color-opponent cells assigned to RGC groups G_{24} and G_{27}, dye-filled and reconstructed subsequent to imaging experiments. Lines for side-view of

morphology and stratification profile indicate On and Off ChAT bands. Arrows point at axon present only for RGCs and not for dACs. **c,** Mean full-field chirp responses (black, s.d. shading in grey; n=5 trials) of RGC groups shown in (b). **d,** Box plots show distribution of expected percentages of color-opponent cells given center *SC* and SC_{Diff} values in each group (for details, see Methods). Black circles indicate true percentage of color-opponent cells. Arrows pointing down- and up indicate groups with significantly more and less color-opponent cells than expected, respectively.

Ventral color-opponent RGCs were assigned to diverse functional groups, including Off, On-Off and On groups (Fig. 7a). Most RGC groups (20/32) contained at least a few (n≥3) color-opponent cells, indicating that color-opponency may partially be inherited from BCs (*cf.* Fig. 4). Surprisingly, the fraction of color-opponent cells greatly varied across groups: Most color-opponent RGCs were assigned to groups displaying slow On responses. For example, many sustained On alpha cells (G_{24}) showed color-opponent responses (Fig. 7a-c), consistent with an earlier study (Chang et al., 2013). In addition, color-opponency was a prominent feature in G_{27}, which exhibited a bistratified morphology (Fig. 7b, Suppl. Fig. S7), reminiscent of RGC type 73 in (Bae et al., 2018). In contrast to BCs, where Off cells were more likely to be color-opponent than On cells, most Off as well as transient On RGC groups contained only few color-opponent cells. This difference between BCs and RGCs suggests that RGC color-opponency is not only inherited from BCs (Discussion).

The most parsimonious explanation for such RGC type-dependent differences in fraction of color-opponent cells is that groups differ in their center and surround spectral preference, with a larger difference between these two preferences resulting in more color-opponent cells. Additionally, non-linear integration of center and surround chromatic information could lead to pronounced color-opponency in specific RGC groups. To distinguish between these two possibilities, we tested how well the percentage of color-opponent cells within a group was explained by its chromatic preference using a permutation test: For each group with >10 assigned cells (27/32), we generated a distribution of expected percentages of color-opponent cells – given the cells' center and surround preference, but shuffling their group labels – and compared it to the observed percentage of color-opponent cells (Fig. 7d; Methods). We found that in approx. 60% (16/27) of all RGC groups investigated, the number of color-opponent cells was explained by the difference in chromatic preference between center and surround. However, the remaining groups showed either a significantly lower or higher percentage of color-opponent cells than expected, indicative of non-linear integration of center and surround chromatic responses in these groups. The seven groups with fewer color-opponent cells (G_2, G_4, G_8, G_{17}, G_{18}, G_{31}, G_{32}) comprised a heterogeneous set of RGC groups, including Off, transient On and contrast suppressed ones (Fig. 7d). In contrast, the four groups with higher percentages of color-opponent cells than expected all showed slow On responses (G_{22}, G_{24}, G_{26}, G_{27}). Interestingly, also the three dAC groups with significantly more color-opponent cells than expected showed slow On responses (Suppl. Fig. S6), which might hint at a common circuit mechanism.

In summary, our data showed that color-opponency is a widespread feature among ventral RGC groups that is partially inherited by presynaptic BC circuits. However, we found evidence for non-linear integration of chromatic information in a subset of RGC groups, increasing the diversity of chromatic responses at the level of the retinal output.

DISCUSSION

Here, we systematically surveyed chromatic signaling across three consecutive processing stages in the mouse retina by population imaging of the chromatic output signals of cones, BCs and RGCs. We showed how color-opponency present in the ventral retina is already created at the cone synapse by lateral inhibition from HCs that is at least partially driven by rod photoreceptors. In addition, we demonstrated that the population of BCs then relays the chromatic information to RGCs in the inner retina, where type-specific, non-linear center-surround interactions result in specific color-opponent output channels to the brain. Our finding that color-opponency is mostly limited to the S-opsin dominant ventral retina is consistent with behavioral experiments suggesting that color vision in mice may be largely restricted to their upper visual field (Denman et al., 2018).

Chromatic processing at the first synapse of the mouse visual system

Many non-mammalian vertebrate species show selective wiring between distinct types of cones and HCs, which generates color-opponent responses already in the outer retina (reviewed in (Baden and Osorio, 2019; Thoreson and Dacey, 2019)). Also in the primate retina, color-opponency emerges already at the photoreceptor synapse. Here, two types of HC that preferentially contact S- or L/M-cones (Dacey et al., 1996; Chan and Grünert, 1998) provide a chromatically opponent antagonistic surround to cones (Packer et al., 2010; Crook et al., 2011). In contrast, mice and some other mammalian species only possess one HC type (Peichl and González-Soriano, 1994; Peichl et al., 1998). As it indiscriminately contacts S- and M-cones, its role in chromatic processing has been much less clear. By recording the glutamatergic output of cones in the intact, whole-mounted retina, we were able to demonstrate that also in mouse color-opponency is already present at the level of the cone output. Specifically, UV-sensitive cones located in the ventral mouse retina exhibited green-sensitive surround responses, mediated by rod-signals that are relayed to cones via HCs. This is consistent with a recent study showing that color-opponent responses of ventral JAM-B RGCs originate from a rod-cone opponent mechanism involving HCs (Joesch and Meister, 2016). The prerequisites for this rod-mediated mechanism have been experimentally established: First, mouse rods can drive visual responses at the low photopic light levels used in our experiments (Tikidji-Hamburyan et al., 2017) and, second, rod signals travel in HCs from the axon terminals to the soma via the HC axon ((Szikra et al., 2014); but see (Trümpler et al., 2008)).

In the following, we discuss three observations made while recording light-evoked responses from cones in the retinal whole-mount preparation.

First, our data suggest that the recorded glutamate signals in the OPL depict cone, but not rod signals. First, our functionally defined ROIs formed regular mosaics resembling that of the anatomical cone array (Behrens et al., 2016). Second, the ROIs co-localized with anatomically identified cone terminals. Third, we did not observe any green-sensitive hyperpolarizing responses upon center stimulation in the ventral retina, as would be expected if glutamatergic output of rod axon terminals contributed to the recorded signals. Why we did not pick up rod signals may be because of differences in the number of vesicles released (Rabl et al., 2005) and number of ribbon synapses (e.g. (Carter-Dawson and LaVail, 1979)) between rods and cones. As a result, the amount of glutamate released by individual rod axon terminals may be below the detection threshold of iGluSnFR.

Second, a fraction of cones in our dataset did not exhibit antagonistic surround responses; this was more often the case for dorsal than ventral cones. It is unlikely that cone-to-cone differences in HC input contribute to the strong variations in surround strengths, as HCs form highly stereotypic connections with each cone's axon terminal (e.g. (Chun et al., 1996; Haverkamp et al., 2000)). Previous studies have demonstrated that the strength of HC feedback depends on functional cone properties, such as membrane potential (Verweij et al., 1996) and adaptational state (e.g. (Burkhardt, 1995)), which might vary between cells. We controlled for experimental parameters such as temperature and scan field size, while other parameters like biosensor expression and therefore laser power applied could have somewhat varied across recording fields and/or retinal locations. It is conceivable that these factors affected surround strengths in cone RFs.

Third, most UV-sensitive cones in both ventral and dorsal retina exhibited decreases in glutamate release to both center and surround UV stimulation. This was not the case for green-sensitive cones, which showed an increase in glutamate release when presenting a UV surround annulus. The effect observed in UV-cones could be explained by lateral signal spread due to specific cone-cone coupling (DeVries et al., 2002; Feigenspan et al., 2004) between UV-cones. Such differential coupling between different cone types has been identified in the primate retina (Hornstein et al., 2004); however, evidence for a similar mechanism in the mouse retina is missing. Alternatively, the sign-conserving surround response of UV-cones might be related to the higher sensitivity of S- compared to M-opsin expressing cones (Baden et al., 2013). Specifically, the intensity of light arising from the surround stimulus scattered within the retina may suffice to drive S-opsin but not M-opsin expressing cones.

Mechanisms generating color-opponency in the mouse retina

Depending on the mechanism used, retinal circuits extracting chromatic information can be roughly classified into two categories. "Cone type-selective pathways" rely on selective wiring of spectrally different cone types to their postsynaptic partners. In contrast, in "cone type-unselective" circuits, color-opponency generally arises as a "side-effect" of other mechanisms, such as center-surround RFs. In the following, we will summarize the evidence for each mechanism in the mouse retina and relate them to our results.

Cone type-selective mechanisms

Usually, cone type-selective retinal circuits depend on BC types that preferentially sample from specific spectral cone types. The best described example for such a cone type-selective pathway is likely the circuit generating blue-yellow opponency in the primate retina. Here, the so-called small bistratified RGC receives blue-On and yellow-Off input from BCs that exclusively contact and largely avoid S-cones, respectively (Dacey and Lee, 1994; Crook et al., 2009b). Cone type-selective BCs have also been identified in most dichromatic mammals (reviewed in (Puller and Haverkamp, 2011)). For example, mice possess an On BC type exclusively contacting S-cones (type 9) and an Off BC type that prefers M-cones (type 1) (Haverkamp et al., 2005; Breuninger et al., 2011; Behrens et al., 2016). Therefore, in dorsal scan fields we expected to find UV-dominant center responses in the innermost IPL layer, where S-cone selective type 9 BCs stratify (Haverkamp et al., 2005; Behrens et al., 2016). However, we found such responses only rarely. The low frequency of presumed type 9 BC responses resonates well with their very sparse axonal arbors. Based on EM data we estimated to find ~1 ribbon synapse per IPL scan field (*cf.* Fig. 4f in (Zhao et al., 2019)). In

addition, we did not observe a bias for purely green center responses in the Off sublamina of dorsal scan fields, as would be expected for M-cone preferring type 1 BCs (Breuninger et al., 2011; Behrens et al., 2016). This may be explained by a relatively small difference in chromatic preference of type 1 compared to other BC types (*cf.* Fig. 6 in (Breuninger et al., 2011)).

In primates, cone type-selective BCs provide separate chromatic input channels to RGCs, generating a center-opponent RF structure (Dacey and Lee, 1994; Crook et al., 2009b). In dichromatic mammals, a similar mechanism results in center-opponent RGCs in ground squirrel (Sher and DeVries, 2012) and likely guinea pig (Yin et al., 2009) and rabbit (Mills et al., 2014). Such a circuit could also exist in mice – at least in the dorsal retina where opsin co-expression is low. However, center-opponent RGC RFs were rare in our dataset and did not comprise a single functional type. For identifying center opponency, the stimulus should ideally be aligned to the RF center of the recorded cell. However, this is not possible in our population approach, where the stimulus is aligned to the center of each recording field (Methods), resulting in a spatial offset of up to 50 µm between stimulus and RF center of the recorded cell. Therefore, we might have underestimated the number of center-opponent RGCs. Until now, there is evidence for only one mouse RGC type that uses cone type-selective BC input: It features a UV-dominant center and a green surround, with the former generated by a bias for connecting to type 9 BCs (Stabio et al., 2018). Therefore, connectivity matrices (e.g. (Helmstaedter et al., 2013; Kim et al., 2014; Behrens et al., 2016)) obtained from large-scale EM reconstructions may result in further candidate cone type-selective pathways.

Cone type-unselective mechanisms

Red-green opponency in the primate retina does not rely on cone type-selective BCs. Instead, it is a consequence of midget RGCs receiving input from one or very few M- and L-cones, resulting in either green- or red-dominant center RFs, that are compared to a yellow (M+L) surround (Martin et al., 2001; Buzás et al., 2006; Field et al., 2010; Crook et al., 2011). Similarly, two color-opponent pathways independent of cone type-selective connectivity have been identified in the mouse retina. First, the asymmetric opsin distribution can result in color-opponent responses of RGCs located along the horizontal midline due to chromatically distinct input to their center and surround (Chang et al., 2013). Second, a rod-cone opponent pathway has been linked to color-opponency in JAM-B RGCs located in the S-opsin dominated ventral retina (Joesch and Meister, 2016). Our results suggest that the latter mechanism is not restricted to a single RGC type, but that most color-opponent responses in the mouse retina are inherited from the outer retina, making color-opponency a widespread feature of ventral neurons.

In line with this, we found that the complete population of ventral BCs conveyed chromatic information to downstream circuits. Interestingly, the difference in center and surround chromatic preference and, therefore, the number of color-opponent responses was larger for Off compared to On BCs. The BCs' inhibitory surround could originate from HCs and/or GABAergic wide-field ACs in the outer and inner retina, respectively. We found that in the ventral retina the surround mediated by HCs is largely green-sensitive. In contrast, the surround mediated by ACs is likely UV-sensitive, as wide-field ACs receive their excitatory drive from BC center responses (e.g. (Olveczky et al., 2003; Murphy-Baum and Taylor, 2015)), which, in the ventral retina, are UV-dominant. Therefore, the more pronounced color-opponency in Off BCs may be due to a stronger contribution of HCs compared to ACs

in generating the Off BCs' inhibitory surround. Surprisingly, this difference between On and Off BCs was not preserved at the level of the retinal output. Here, many Off RGC groups contained fewer color-opponent cells than expected from their center and surround chromatic preference. In contrast, color-opponency was significantly enriched in some slow On RGC and dAC groups. This indicates that center and surround component of RGC RFs might be driven by different BC circuits. For example, a color-opponent slow On RGC may receive center excitation from non-opponent On BCs and surround inhibition from sign-inverting ACs driven by opponent Off BCs. However, as the size of the center stimulus used for IPL and GCL recordings was different, explaining exactly how observed RGC responses arise from recorded BC responses requires further investigation.

In summary, our data provide little evidence for cone type-selective circuits in the mouse retina. Instead, most color-opponent responses originate in the outer retina, likely generated by a rod-cone opponent pathway. In the inner retina, chromatic information from cones is further processed, resulting in type-specific chromatic responses at the level of the retinal output.

Functional relevance of color-opponency in mice

The asymmetric opsin distribution divides the mouse retina into distinct regions. The dorsal part resembles the cone mosaic of other dichromatic mammals, with many M-cones and few S-cones (Ahnelt et al., 2006). Therefore, one would expect that the evolutionary conserved circuits that extract blue-green opponency (reviewed in (Thoreson and Dacey, 2019)) also exist in the dorsal retina of mice. In contrast, the ventral part of the mouse retina, with its M-cones co-expressing S-opsin (Röhlich et al., 1994; Applebury et al., 2000), was long considered unfit for color vision. Instead, it was linked to optimal sampling of achromatic contrast information in the sky portion of natural scenes (Baden et al., 2013). We here show that in fact, color-opponent neurons are predominantly located in the ventral retina of mice. This is in agreement with previous RGC studies (Chang et al., 2013; Joesch and Meister, 2016) as well as with a recent behavioral study, which demonstrated that mice perform much better in discriminating colored light spots presented in their upper visual field (Denman et al., 2018). Using a rod-cone based mechanism to extract chromatic information in the ventral retina may be actually advantageous, because it allows color vision (Denman et al., 2018) and detecting dark objects such as predatory birds (Baden et al., 2013) through the widespread expression of S-opsin. This arrangement might also be relevant in other species with a regional increase in S-opsin density in their retina (reviewed in (Peichl, 2005)), including the common shrew (Peichl et al., 2000) or some hyenas (Calderone et al., 2003). Because mouse rod photoreceptors are active in the photopic regime (Tikidji-Hamburyan et al., 2017), rod-cone opponency likely contributes to the animal's color vision across a substantial intensity range, increasing its relevance for informing behavior.

According to the efficient coding theory, sensory systems adapt to the distribution of signals present in their natural environment (Barlow and BH, 1961). That color-opponency of mice appears to be largely restricted to their ventral retina suggests that behaviorally relevant chromatic information should be found in their upper visual field. It has been speculated that mice use color vision for social communication by detecting urine tags (Joesch and Meister, 2016). However, urine tags large enough to appear in the upper visual field have so far only been observed for mice housed under unnatural conditions (Welch, 1953). In addition, urine might not constitute a reliable visual cue under natural conditions (Lind et al., 2013), especially since mice olfaction would be the more obvious choice to detect and analyse urine

570 cues. Alternatively, as most predators are expected to approach the mouse from above, color
571 vision in the upper visual field could well support threat detection. Especially for visual scenes
572 with inhomogeneous illumination (e.g. forrest), that result in large intensity fluctuations at the
573 photoreceptor array, color-opponent RF structures may result in a more reliable signal
574 (discussed in (Maximov, 2000; Kelber et al., 2003)).

575

METHODS

Animals and tissue preparation

All animal procedures adhered to the laws governing animal experimentation issued by the German Government. For all experiments, we used 5- to 18-week-old mice of either sex. For OPL recordings, we used $Cx57^{+/+}$ (n = 9; (Ströh et al., 2013)) mice, which were negative for Cre recombinase on both alleles and, therefore, could be considered wild-type animals. In addition, we used the HR2.1:TN-XL (n = 3) mouse line where the calcium indicator TN-XL was exclusively expressed in cones (Suppl. Fig. S8) (Wei et al., 2012). For IPL recordings, we used $ChAT^{Cre}$ (n = 5, JAX 006410, The Jackson Laboratory; (Rossi et al., 2011)) mice and for GCL recordings we used C57Bl/6 (n = 11, JAX 000664) or $Pvalb^{Cre}$ (n = 9, JAX 008069; ((Hippenmeyer et al., 2005)) mice. The transgenic lines $ChAT^{Cre}$ and $Pvalb^{Cre}$ were crossbred with the Cre-dependent red fluorescent reporter line $Ai9^{tdTomato}$ (JAX 007905). Owing to the exploratory nature of our study, we did not use randomization and blinding. No statistical methods were used to predetermine sample size.

Animals were housed under a standard 12 h day/night rhythm. For activity recordings, animals were dark-adapted for ≥1 h, then anaesthetized with isoflurane (Baxter) and killed by cervical dislocation. The eyes were enucleated and hemisected in carboxygenated (95% O^2, 5% CO^2) artificial cerebrospinal fluid (ACSF) solution containing (in mM): 125 NaCl, 2.5 KCl, 2 $CaCl_2$, 1 $MgCl_2$, 1.25 NaH_2PO_4, 26 $NaHCO_3$, 20 glucose, and 0.5 L-glutamine (pH 7.4). Then, the tissue was either electroporated (see below) or moved to the recording chamber, where it was continuously perfused with carboxygenated ACSF at ~36 °C. In all experiments, ACSF contained ~0.1 µM Sulforhodamine-101 (SR101, Invitrogen) to reveal blood vessels and any damaged cells in the red fluorescence channel (Euler et al., 2009). All procedures were carried out under very dim red (>650 nm) light.

Bulk electroporation

For recordings in the ganglion cell layer (GCL), the fluorescent calcium indicator Oregon-Green BAPTA-1 (OGB-1) was bulk electroporated as described before (Briggman and Euler, 2011; Baden et al., 2016). In brief, the retina was dissected from the eyecup, flat-mounted onto an Anodisc (#13, 0.2 µm pore size, GE Healthcare) with the GCL facing up, and placed between two 4-mm horizontal plate electrodes (CUY700P4E/L, Nepagene/Xceltis). A 10 µl drop of 5 mM OGB-1 (hexapotassium salt; Life Technologies) in ACSF was suspended from the upper electrode and lowered onto the retina. After application of 9 pulses (~9.2 V, 100 ms pulse width, at 1 Hz) from a pulse generator/wide-band amplifier combination (TGP110 and WA301, Thurlby handar/Farnell), the tissue was moved to the recording chamber of the microscope and left to recover for ~30 minutes before the recordings started.

Virus injection

The viral construct AAV2.7m8.hSyn.iGluSnFR was generated in the Dalkara lab as described previously (Dalkara et al., 2013; Khabou et al., 2016). The iGluSnFR plasmid construct was provided by J. Marvin and L. Looger (Janelia Research Campus, USA). A volume of 1 µl of the viral construct was then injected into the vitreous humour of 3- to 8-week-old mice anaesthetized with 10% ketamine (Bela-Pharm GmbH & Co. KG) and 2% xylazine (Rompun, Bayer Vital GmbH) in 0.9% NaCl (Fresenius). For the injections, we used a micromanipulator (World Precision Instruments) and a Hamilton injection system (syringe: 7634-01, needles:

207434, point style 3, length 51 mm, Hamilton Messtechnik GmbH). Imaging experiments were performed 3–4 weeks after injection. As iGluSnFR expression tended to be weaker in the central retina, most OPL and IPL scan fields were acquired in the medial to peripheral ventral or dorsal retina.

Two-photon imaging

We used a MOM-type two-photon microscope (designed by W. Denk, MPI, Heidelberg; purchased from Sutter Instruments/Science Products). The design and procedures have been described previously (Euler et al., 2009). In brief, the system was equipped with a mode-locked Ti:Sapphire laser (MaiTai-HP DeepSee, Newport Spectra-Physics), two fluorescence detection channels for iGluSnFR/OGB-1 (HQ 510/84, AHF/Chroma) and SR101/tdTomato (HQ 630/60, AHF), and a water immersion objective (W Plan-Apochromat 20× /1.0 DIC M27, Zeiss). The laser was tuned to 927 nm for imaging iGluSnFR, OGB-1 or SR101, and to 1,000 nm for imaging tdTomato. For image acquisition, we used custom-made software (ScanM by M. Müller and T.E.) running under IGOR Pro 6.3 for Windows (Wavemetrics), taking time-lapsed 64 × 64 pixel image scans (at 7.8125 Hz) for OGB-1 imaging in the GCL and 128 × 128 pixel image scans (at 3.9 Hz) for glutamate imaging in the outer plexiform layer (OPL). For vertical glutamate imaging in the IPL, we recorded time-lapsed 64 x 56 pixel image scans (at 11.16 Hz) using an electrically tunable lens as described previously (Zhao et al., 2019). For high resolution images, 512 x 512 pixel images were acquired. The positions of the fields relative to the optic nerve were routinely recorded.

Two-photon imaging introduces a constant laser-induced baseline activity (see below and (Euler et al., 2009, 2019)). While we found that green-sensitive cones in the mouse were somewhat more affected by this “background illumination”, this slight bias did not change the conclusions of this study (Suppl. Fig. S9).

Light stimulation

For light stimulation, we used two different systems. The first system focused a DLP projector (‘lightcrafter’ (LCr), DPM-E4500UVBGMKII, EKB Technologies Ltd) with internal UV and green light-emitting diodes (LEDs) through the objective (TTO). To optimize spectral separation of mouse M- and S-opsins, LEDs were band-pass filtered (390/576 Dualband, F59-003, AHF/Chroma). The second system used an LCr with a lightguide port (DPM-FE4500MKIIF) to couple in external, band-pass filtered UV and green LEDs (green: 576 BP 10, F37-576; UV: 387 BP 11, F39-389; both AHF/Chroma), focused through the condenser (TTC) of the microscope (for details, see (Franke et al., 2019)). For glutamate recordings in the IPL, we solely used the TTO stimulator, while for OPL and GCL recordings we used both TTO and TTC. LEDs were synchronized with the microscope’s scan retrace. Stimulator intensity (as photoisomerization rate, 10^3 P* per s per cone) was calibrated as described previously (Franke et al., 2019) to range from ~0.5 (black image) to ~20 for M- and S-opsins, respectively. In addition, a steady illumination component of ~10^4 P* per s per cone was present during the recordings because of two-photon excitation of photopigments (discussed in (Euler et al., 2009, 2019; Baden et al., 2013)). The light stimulus was centered to the recording field before every experiment. For all experiments, the tissue was kept at a constant mean stimulator intensity level for at least 15 s after the laser scanning started and before light stimuli were presented.

Two types of light stimuli were used for glutamate imaging in the OPL:

(a) full-field (700 µm in diameter) UV and green flashes,

(b) center (150 µm in diameter) and surround (annulus; full-field flashes sparing the central 150 µm) UV and green flashes.

Three types of stimuli were used for glutamate imaging in the IPL:

(c) local (100 µm in diameter) chirp (for details, see (Franke et al., 2017));

(d) 2 Hz sine-wave modulation of center and surround for UV and green LED; and

(e) a UV and green center-surround flicker stimulus, with intensity of center and surround determined independently by a balanced 180-s random sequence at 10 Hz.

Three types of stimuli were used for calcium imaging in the GCL:

(f) full-field (700 µm in diameter) chirp stimulus (for details, see (Baden et al., 2016));

(g) 0.3 × 1 mm bright bar moving at 1 mm s^{-1} in eight directions (Briggman and Euler, 2011); and

(h) a UV and green center-surround flicker stimulus (250 µm in diameter for center), with intensity of center and surround determined independently by a balanced 300-s random sequence at 5 Hz.

For recording calcium responses in HR2.1:TN-XL mice, we used full-field white flashes (2 s, 50% duty cycle). Sizes of center stimuli were selected to completely fill the scan field area of the recordings and, therefore, did not correspond to RF center sizes of retinal neurons.

Pharmacology

All drugs were bath applied for at least 10 min before recordings. The following drug concentrations were used: 50 µM 6,7-dinitroquinoxaline-2,3-dione (NBQX), ACSF with twice the normal concentration of KCl (5 mM). Drug solutions were carboxygenated and warmed to ~ 36 °C before application.

Single-cell electrophysiology

GCL cells were targeted using an infrared LED and CCD camera for intracellular recordings. Electrodes were pulled on a P-1000 micropipette puller (Sutter Instruments) with resistances of ~7-15 MΩ and filled with solution consisting of (in mM): 120 K-gluconate, 5 NaCl, 10 KCl, 1 MgCl2, 1 EGTA, 10 HEPES, 2 Mg-ATP, and 0.5 Tris-GTP, adjusted to pH 7.2 using 1 M KOH. Data were acquired using an Axopatch 200B amplifier in combination with a Digidata 1440 (both: Molecular Devices), digitized at 20 kHz and analyzed offline using Igor Pro (Wavemetrics). For recordings, we targeted GCL cells located in the medial retina allowing to investigate the effect of the two-photon laser on both UV and green responses.

Single cell injection and morphology reconstruction

OGB-1-labelled GCL cells were targeted with electrodes (~5-15 MΩ) subsequent to two-photon recordings. Single cells in the GCL were dye-filled with SR101 (Invitrogen) using the buzz function (100-ms pulse) of the MultiClamp 700B software (Molecular Devices). Pipettes were carefully retracted as soon as the cell began to fill. Approximately 20 min were allowed for the dye to diffuse throughout the cell before imaging started. After recording, an image stack was acquired to document the cell's morphology, which was then traced

semi-automatically using the Simple Neurite Tracer plugin implemented in Fiji (https://imagej.net/Simple_Neurite_Tracer). In cases of any warping of the IPL, as described before (Baden et al., 2016), we used the original image stack to correct the traced cells using custom-written scripts in IGOR Pro.

Data analysis

Data analysis was performed using IGOR Pro. Upon publication, all data will be available at www.retinal-functomics.org.

Pre-processing

For GCL recordings, ROIs were defined semi-automatically by custom software as described before (Baden et al., 2016). For glutamate imaging in OPL and IPL, ROIs were defined automatically by custom correlation-based algorithms in IGOR Pro. Here, ROI sizes were restricted to match the sizes of cone (3-7 µm diameter) and BC axon terminals (1-4 µm diameter) in OPL and IPL scans, respectively. For OPL recordings, a specific correlation threshold for each scan field was manually selected to account for differences in staining and signal-to-noise-ratio. For IPL recordings, correlation thresholds were determined automatically and varied across the IPL due to differences in iGluSnFR labeling and laser intensity (for details, see (Zhao et al., 2019)). For every ROI located in the IPL, depth was determined using the shortest distance of ROI center to TdT-labeled ChAT bands and normalized such that 0 and 1 corresponded to On and Off ChAT band, respectively.

To relate each ROIs functional properties to its location on the retina, we registered the orientation of the retina for all IPL and GCL recordings and calculated the linear distance of each ROI to the optic nerve. For most OPL recordings, we did not register the retinal orientation. Here, we used the previously described gradient in opsin expression (Applebury et al., 2000; Baden et al., 2013) to separate dorsal (mean center $SC > 0$) and ventral (mean center $SC < 0$) scan fields.

The glutamate or calcium traces for each ROI were extracted (as Δ F/F) using custom analysis code based on the image analysis toolbox SARFIA for IGOR Pro (Dorostkar et al., 2010) and resampled at 500 Hz. A stimulus time marker embedded in the recorded data served to align the traces relative to the visual stimulus with 2 ms precision. For this, the timing for each ROI was corrected for sub-frame time-offsets related to the scanning.

First, we de-trended the traces by high-pass filtering above ~0.1 Hz. For all stimuli except for the center-surround flicker, we then computed the median activity r(t) across stimulus repetitions (n=4-5 repetitions for chirps, n=3 repetitions for sine, n=25-30 repetitions for full-field and center-surround flashes, n=3 repetitions for moving bars).

Center-surround stimulus and event kernels

We mapped the stimulus kernels to the center-surround flicker by computing the glutamate/calcium event-triggered average (“event-triggered stimulus kernels”). To this end, we differentiated the response trace and estimated a response threshold as:

$$\sigma = \frac{median(|r(t)|)}{0.6745} \quad (1)$$

We then computed the glutamate/calcium transient-triggered average stimulus, weighting each sample by the amplitude of the transient:

$$\mathbf{F}(x,y,\tau) = \frac{1}{M}\sum_{i=1}^{M}\mathbf{c}(t_i)\mathbf{S}(x,t_i+\tau) \quad (2)$$

Here, $\mathbf{S}(x,t_i+\tau)$ is the stimulus, τ is the time lag and *M* is the number of glutamate/calcium events.

Similarly, for estimating the average glutamate/calcium event kernel upon full-field stimulation, we first identified time points of full-field activation in the stimulus trace and then computed the stimulus-triggered average glutamate/calcium event ("stimulus-triggered event kernels").

Response quality indices

Kernel quality (Qi_{Kernel}) was measured by comparing area under the curve (F_{Area}) of each response kernel with the respective baseline:

$$Qi_{Kernel} = 1 - \frac{|F_{Area(Baseline)}|}{|F_{Area(Kernel)}|} . \quad (3)$$

Event quality (Qi_{Event}) was measured by comparing area under the curve (F_{Area}) of each event with the respective baseline:

$$Qi_{Event} = 1 - \frac{|F_{Area(Baseline)}|}{|F_{Area(Event)}|} . \quad (4)$$

To measure how well a cell responded to the other stimuli used (chirp, sine modulation, full-field and center-surround flashes, moving bars), we computed the signal-to-noise ratio

$$Qi = \frac{Var[(C)r]t}{(Var[C]t)r} \quad (5)$$

where C is the T by R response matrix (time samples by stimulus repetitions), while $()_x$ and $Var[]_x$ denote the mean and variance across the indicated dimension, respectively (Baden et al., 2016; Franke et al., 2017).

For further analysis of chromatic responses, we used

(a) ROIs in the OPL if they showed hyperpolarizing center or full-field responses and $Qi_{full\text{-}field} > 0.25$ (n=2,132/2,945) or $Qi_{center\text{-}surround} > 0.25$ (n=2,008/2,589). For analysis of surround responses, only ROIs with an antagonistic response showing an increase in glutamate release with $F_{Area(Surround)} > (|F_{Area(Center)}|/10)$ were considered (n=1,057/2,589).

(b) ROIs in the IPL if $Qi_{Kernel} > 0.6$ for center UV or green stimulus kernel (n=3,188/3,604).

(c) ROIs in the GCL if $Qi_{Kernel} > 0.6$ for center UV or green stimulus kernel (n=n=5,922/8,429). For group assignment of GCL cells, we in addition only used ROIs with $Qi_{Chirp} > 0.4$ or $Qi_{Bars} > 0.6$ (n=4,519/8,429). In addition, we excluded scan fields for which less than 50% of all cells passed the above mentioned quality thresholds (n=2 scan fields).

Spectral contrast

For estimating the chromatic preference of recorded cells, we computed a spectral contrast (*SC*) using the area-under-the-curve (F_{Area}) of the mean glutamate traces (OPL recordings; *cf.*

Fig. 1e,g) or the center-surround stimulus kernels (IPL and GCL recordings; *cf.* Figs. 3d, 5c). For stimulus kernels of IPL and GCL ROIs, we first estimated absolute F_{Area} of each of the four conditions (UV and green center and surround) and then set F_{Area} estimated from kernels anticorrelated to the center kernel to negative values (e.g. antagonistic surround will have negative F_{Area}).

Previously, *SC* has been estimated as Michelson contrast based on dendritic calcium signals in mouse HCs (Chapot et al., 2017), ranging from -1 to 1 for the cell responding solely to UV and green, respectively. However, this requires UV and green responses to have the same response polarity (e.g. only decreases in calcium to full-field responses (Chapot et al., 2017)). As both center and surround responses of cells in OPL, IPL and GCL recordings can have different response polarities to UV and green, we here distinguished three cases to estimate *SC*.

If green and UV responses had the same response polarity (e.g. cone (1) in Fig. 1e), *SC* was estimated as Michelson contrast:

$$SC = \frac{|F_{Area(Green)}| - |F_{Area(UV)}|}{|F_{Area(Green)}| + F_{Area(UV)}|} \quad (6\text{-a})$$

If the green response had an expected response polarity (e.g. increase in glutamate release upon surround stimulation in cones; cone (2) in Fig. 1l) and the UV response was antagonistic, *SC* was estimated as

$$SC = 1 + \frac{|F_{Area(UV)}|}{|F_{Area(Green)}|} \quad (6\text{-b})$$

Similarly, if the UV response had an expected response polarity and the green response was antagonistic, *SC* was estimated according to

$$SC = -1 - \frac{|F_{Area(Green)}|}{|F_{Area(UV)}|} \; . \quad (6\text{-c})$$

For estimating the difference in *SC* between center and surround (SC_{Diff}), we used:

$$SC_{Diff} = SC_{Surround} - SC_{Center}. \quad (7)$$

Density recovery profiles

To estimate density recovery profiles (DRPs; (Rodieck, 1991)) of OPL ROI masks, we first calculated the distance of each ROI to each other ROI within the scan field, binned the distances (bin size=2 µm) and normalized each bin count to the bin area. Next, we estimated the mean DRP per scan field by averaging the histograms of all ROIs within a field (n=56 ± 30 ROIs per scan field). To obtain the mean DRPs of all ROI masks, we used n=52 scan fields.

For relating DRPs of the ROIs to anatomy, we used a recent EM dataset of reconstructed cone and rod terminals to estimate anatomical DRPs as described above (*cf.* Suppl. Fig. S1; n=163/2095 cone/rod terminals; (Behrens et al., 2016)). For calculating a cone DRP with 3% rods (*cf.* Suppl. Fig. S1d), we first calculated the density of rod terminals and then randomly placed 3% of the expected number of rod terminals across the reconstructed area.

Field entropy

Field entropy (S_{Field}) was used to estimate the variability of chromatic tuning within single IPL and GCL scan fields (Suppl. Fig. S4). First, *SC* values of all ROIs within one scan field were binned (bin size: 0.2) and then S_{Field} was defined as

$$S_{Field} = -\sum_i p_i \log_2 p_i \quad (8)$$

where i is the number of *SC* bins and p_i corresponds to the number of ROIs in the i^{th} bin. S_{Field} = 0 if all ROIs of one recording field are in the same *SC* bin and therefore have the same spectral tuning. S_{Field} increases if ROIs are equally distributed across multiple bins. In general, high field-entropy indicates high chromatic tuning heterogeneity within a single field. As the number of ROIs per scan field was larger for IPL than GCL recordings, we likely underestimated the difference in S_{Field} between IPL than GCL recordings.

Full-field opponency

To measure whether UV and green full-field responses were color-opponent, we calculated the linear correlation coefficient (ρ) between UV and green event kernels. For further analysis of opponent cells (*cf.* Figs. 3f, 4f), we only used ROIs with ρ<-0.3 and QI_{Event}>0.25.

Sine data

To estimate the chromatic preference of a cell based on its response to sinusoidal modulation (Suppl. Fig. S3), we first quantified the response phase for every stimulus condition (UV and green center and surround). For every ROI, we cross-correlated the mean glutamate trace of each condition with the stimulus trace and converted the time shift of maximal correlation into degrees. We then extracted the amplitude of the fundamental response component (F1) from the mean glutamate traces using Fourier transform. For the polar plot, response phases of different ROIs were binned using a bin size of 15° and each polar histogram was normalized according to its mean F1 amplitude. We performed this analysis for ventral and dorsal On (IPL depth < 0.2) and Off (IPL depth > 0.5) ROIs separately.

Direction selectivity

Direction selectivity (DS) of recorded GCL cell was computed as described before (Baden et al., 2016). In brief, we first performed singular value decomposition (SVD) on the mean response matrix (time samples by number of directions) of each cell. This decomposes the response into a temporal component and a direction dependent component or tuning curve. An advantage of this procedure is that it does not require manual selection of time bins for computing direction tuning but extracts the direction-tuning curve given the varying temporal dynamics of different neurons.

To measure DS, we computed the vector sum in the 2D plane and used the resulting vector length as DS index. We additionally assessed the statistical significance of direction tuning using a permutation test (Ecker et al., 2014). Here, we created surrogate trials by shuffling the trial labels, computing the tuning curve and vector sum for each surrogate trial. Carrying out this procedure 1,000 times generated a null distribution, assuming no direction tuning. We used the percentile of the true vector length as the P value for the direction tuning.

Clustering of GCL cells

The pre-processed ROI traces of GCL cells (n=n=4,519/8,429) were assigned to previously identified functional RGC cluster (Baden et al., 2016) by identifying for each cell the cluster

with the best matching response properties. To account for a slight mismatch in frame rate for our stimulation systems compared to the previous one, calcium traces were shifted in time (t=40 ms) and smoothed (for chirp stimulus only, boxcar smoothing with n=5 points corresponding to 0.64 s) before calculating the linear correlation coefficients between a GCL cell´s mean trace and all matching cluster mean traces for the chirp and the moving bar stimuli. Specifically, DS cells were correlated with DS clusters, non-DS cells were correlated with non-DS clusters, and alpha cells (soma area > 170 µm^2) were correlated with alpha cell clusters. To combine stimulus-specific correlations and response quality, we generated an overall match index (Mi) of each GCL cell to all RGC clusters (Román Rosón et al., 2019):

$$Mi = \frac{Qi_{Chirp}}{Qi_{Chirp} + Qi_{Bar}} * r_{Chirp} + \frac{Qi_{Bar}}{Qi_{Chirp} + Qi_{Bar}} * r_{Ba}. \quad (9)$$

Finally, each GCL cell with *Mi* > 0.5 was assigned to the cluster with the highest *Mi* and clusters were combined into functional RGC groups as described before (Baden et al., 2016).

Statistical analysis

We used the non-parametric Wilcoxon signed-rank test for quantifying the difference between cone surround responses under control and NBQX conditions (Fig. 2f), and field entropy of IPL and GCL scan fields (Suppl. Fig. S4).

We used the Chi-squared test to compare the distribution of anatomical and functional cone arrays (Suppl. Fig. S1h).

We used a Linear Mixed-Effects Model to analyze the difference between center and surround *SC* for OPL (Fig. 2b,c), IPL (Fig. 4b) and GCL recordings (Fig. 6b). This allowed to incorporate a random effects term in a linear predictor expression accounting for the fact that not all ROIs with a center response displayed a surround response (partially paired data). We used the `lme4`-package for R to implement the model and perform statistical testing (Bates et al., 2015). For details, see “Results of statistical analysis” in Suppl. Information.

We used Generalized Additive Models (GAMs) to analyze the relationship of difference in center and surround *SC* (SC_{Diff}) and IPL depth (Fig. 4e); opponency and IPL depth (Fig. 4f); center chromatic preference (SC_{center}) and IPL depth (Suppl. Fig. S2b). GAMs extend the generalized linear model by allowing the linear predictors to depend on arbitrary smooth functions of the underlying variables (Wood, 2006). In practise, we used the `mgcv`-package for R to implement GAMs and perform statistical testing. For details, see “Results of statistical analysis” in Suppl. Information.

To test if the number of color-opponent cells within single RGC and dAC groups was significantly larger/lower than expected from center *SC* and SC_{Diff}, we used a permutation test (Fig. 7g). First, we binned SC_{Diff} values across all groups (bin size=0.25). For every cell assigned to one group, we then randomly picked a different cell within the same SC_{Diff} bin and with a similar center *SC* (±0.1). Like this, we generated an “across-group” distribution of SC_{Diff} values with similar mean and s.d., but with shuffled cell labels. Then, we estimated the percentage of color-opponent cells in this “across-group” distribution and repeated this procedure for 10,000 times per group, generating a null distribution. Finally, we used the percentile of the true percentage of color-opponent cells as the P value.

REFERENCES

Ahnelt PK, Schubert C, Kübber-Heiss A, Schiviz A, Anger E (2006) Independent variation of retinal S and M cone photoreceptor topographies: A survey of four families of mammals. Vis Neurosci 23:429–435.

Applebury ML, Antoch MP, Baxter LC, Chun LL, Falk JD, Farhangfar F, Kage K, Krzystolik MG, Lyass LA, Robbins JT (2000) The murine cone photoreceptor: a single cone type expresses both S and M opsins with retinal spatial patterning. Neuron 27:513–523.

Baden T, Berens P, Franke K, Román Rosón M, Bethge M, Euler T (2016) The functional diversity of retinal ganglion cells in the mouse. Nature 529:345–350.

Baden T, Osorio D (2019) The Retinal Basis of Vertebrate Color Vision. Annu Rev Vis Sci Available at: http://dx.doi.org/10.1146/annurev-vision-091718-014926.

Baden T, Schubert T, Chang L, Wei T, Zaichuk M, Wissinger B, Euler T (2013) A tale of two retinal domains: near-optimal sampling of achromatic contrasts in natural scenes through asymmetric photoreceptor distribution. Neuron 80:1206–1217.

Bae JA, Mu S, Kim JS, Turner NL, Tartavull I, Kemnitz N, Jordan CS, Norton AD, Silversmith WM, Prentki R, Sorek M, David C, Jones DL, Bland D, Sterling ALR, Park J, Briggman KL, Seung HS, Eyewirers (2018) Digital museum of retinal ganglion cells with dense anatomy and physiology. Cell 173:1293–1306.e19.

Barlow, BH (1961) Possible principles underlying the transformation of sensory messages. In: Sensory Communication. MIT Press.

Bates D, Mächler M, Bolker B, Walker S (2015) Fitting linear mixed-effects models using lme4. Journal of Statistical Software 67:1–48.

Behrens C, Schubert T, Haverkamp S, Euler T, Berens P (2016) Connectivity map of bipolar cells and photoreceptors in the mouse retina. Elife 5:e29941.

Breuninger T, Puller C, Haverkamp S, Euler T (2011) Chromatic bipolar cell pathways in the mouse retina. J Neurosci 31:6504–6517.

Briggman KL, Euler T (2011) Bulk electroporation and population calcium imaging in the adult mammalian retina. J Neurophysiol 105:2601–2609.

Burkhardt DA (1995) The influence of center-surround antagonism on light adaptation in cones in the retina of the turtle. Vis Neurosci 12:877–885.

Buzás P, Blessing EM, Szmajda BA, Martin PR (2006) Specificity of M and L cone inputs to receptive fields in the parvocellular pathway: random wiring with functional bias. J Neurosci 26:11148–11161.

Calderone JB, Jacobs GH (1995) Regional variations in the relative sensitivity to UV light in the mouse retina. Vis Neurosci 12:463–468.

Calderone JB, Reese BE, Jacobs GH (2003) Topography of photoreceptors and retinal ganglion cells in the spotted hyena (Crocuta crocuta). Brain Behav Evol 62:182–192.

Calkins DJ, Tsukamoto Y, Sterling P (1998) Microcircuitry and mosaic of a blue-yellow ganglion cell in the primate retina. J Neurosci 18:3373–3385.

Carter-Dawson LD, LaVail MM (1979) Rods and cones in the mouse retina. I. Structural analysis using light and electron microscopy. J Comp Neurol 188:245–262.

Chang L, Breuninger T, Euler T (2013) Chromatic coding from cone-type unselective circuits in the mouse retina. Neuron 77:559–571.

Chan TL, Grünert U (1998) Horizontal cell connections with short wavelength-sensitive cones

in the retina: a comparison between New World and Old World primates. J Comp Neurol 393:196–209.

Chapot CA, Behrens C, Rogerson LE, Baden T, Pop S, Berens P, Euler T, Schubert T (2017) Local signals in mouse horizontal cell dendrites. Curr Biol 27:3603–3615.e5.

Chun M-H, Grünert U, Martin PR, Wässle H (1996) The synaptic complex of cones in the fovea and in the periphery of the macaque monkey retina. Vision Res 36:3383–3395.

Crook JD, Davenport CM, Peterson BB, Packer OS, Detwiler PB, Dacey DM (2009a) Parallel ON and OFF cone bipolar inputs establish spatially coextensive receptive field structure of blue-yellow ganglion cells in primate retina. J Neurosci 29:8372–8387.

Crook JD, Manookin MB, Packer OS, Dacey DM (2011) Horizontal cell feedback without cone type-selective inhibition mediates “red–green” color opponency in midget ganglion cells of the primate retina. Journal of Neuroscience 31:1762–1772.

Crook JD, Troy JB, Packer OS, Vrieslande JD, Dacey DM (2009b) Contribution of excitatory and inhibitory conductances to receptive field structure in midget and parasol ganglion cells of macaque monkey retina. J Vis 9:57a – 57.

Dacey DM (2000) Parallel pathways for spectral coding in primate retina. Annu Rev Neurosci 23:743–775.

Dacey DM, Lee BB (1994) The “blue-on” opponent pathway in primate retina originates from a distinct bistratified ganglion cell type. Nature 367:731–735.

Dacey DM, Lee BB, Stafford DK, Pokorny J, Smith VC (1996) Horizontal cells of the primate retina: cone specificity without spectral opponency. Science 271:656–659.

Dalkara D, Byrne LC, Klimczak RR, Visel M, Yin L, Merigan WH, Flannery JG, Schaffer DV (2013) In vivo–directed evolution of a new adeno-associated virus for therapeutic outer retinal gene delivery from the vitreous. Sci Transl Med 5:189ra76–ra189ra76.

Denman DJ, Luviano JA, Ollerenshaw DR, Cross S, Williams D, Buice MA, Olsen SR, Reid RC (2018) Mouse color and wavelength-specific luminance contrast sensitivity are non-uniform across visual space. Elife 7:e31209.

DeVries SH, Qi X, Smith R, Makous W, Sterling P (2002) Electrical coupling between mammalian cones. Curr Biol 12:1900–1907.

Dominy NJ, Lucas PW (2001) Ecological importance of trichromatic vision to primates. Nature 410:363–366.

Dorostkar MM, Dreosti E, Odermatt B, Lagnado L (2010) Computational processing of optical measurements of neuronal and synaptic activity in networks. J Neurosci Methods 188:141–150.

Ecker AS, Berens P, Cotton RJ, Subramaniyan M, Denfield GH, Cadwell CR, Smirnakis SM, Bethge M, Tolias AS (2014) State dependence of noise correlations in macaque primary visual cortex. Neuron 82:235–248.

Euler T, Franke K, Baden T (2019) Studying a light sensor with light: Multiphoton imaging in the retina. preprints Available at: https://www.preprints.org/manuscript/201903.0244.

Euler T, Hausselt SE, Margolis DJ, Breuninger T, Castell X, Detwiler PB, Denk W (2009) Eyecup scope—optical recordings of light stimulus-evoked fluorescence signals in the retina. Pflügers Archiv - European Journal of Physiology 457:1393–1414.

Feigenspan A, Janssen-Bienhold U, Hormuzdi S, Monyer H, Degen J, Söhl G, Willecke K, Ammermüller J, Weiler R (2004) Expression of connexin36 in cone pedicles and

OFF-cone bipolar cells of the mouse retina. J Neurosci 24:3325–3334.

Field GD, Gauthier JL, Sher A, Greschner M, Machado TA, Jepson LH, Shlens J, Gunning DE, Mathieson K, Dabrowski W, Paninski L, Litke AM, Chichilnisky EJ (2010) Functional connectivity in the retina at the resolution of photoreceptors. Nature 467:673–677.

Franke K, Berens P, Schubert T, Bethge M, Euler T, Baden T (2017) Inhibition decorrelates visual feature representations in the inner retina. Nature 542:439–444.

Franke K, Chagas AM, Zhao Z, Zimmermann MJY, Qiu Y, Szatko K, Baden T, Euler T (2019) An arbitrary-spectrum spatial visual stimulator for vision research. bioRxiv:649566 Available at: https://www.biorxiv.org/content/10.1101/649566v1.

Gerl EJ, Morris MR (2008) The causes and consequences of color vision. Evolution: Education and Outreach 1:476–486.

Greene MJ, Kim JS, Seung HS, EyeWirers (2016) Analogous convergence of sustained and transient inputs in parallel On and Off pathways for retinal motion computation. Cell Rep 14:1892–1900.

Haverkamp S, Grünert U, Wässle H (2000) The cone pedicle, a complex synapse in the retina. Neuron 27:85–95.

Haverkamp S, Wässle H, Duebel J, Kuner T, Augustine GJ, Feng G, Euler T (2005) The primordial, blue-cone color system of the mouse retina. J Neurosci 25:5438–5445.

Helmstaedter M, Briggman KL, Turaga SC, Jain V, Seung HS, Denk W (2013) Connectomic reconstruction of the inner plexiform layer in the mouse retina. Nature 500:168–174.

Hippenmeyer S, Vrieseling E, Sigrist M, Portmann T, Laengle C, Ladle DR, Arber S (2005) A developmental switch in the response of DRG neurons to ETS transcription factor signaling. PLoS Biol 3:e159.

Hornstein EP, Verweij J, Schnapf JL (2004) Electrical coupling between red and green cones in primate retina. Nat Neurosci 7:745–750.

Huang SC, Chiou TH, Marshall J, Reinhard J (2014) Spectral sensitivities and color signals in a polymorphic damselfly. PLoS One 9:e87972.

Jacobs GH, Neitz J, Deegan JF 2nd (1991) Retinal receptors in rodents maximally sensitive to ultraviolet light. Nature 353:655–656.

Jacobs GH, Williams GA, Fenwick JA (2004) Influence of cone pigment coexpression on spectral sensitivity and color vision in the mouse. Vision Res 44:1615–1622.

Joesch M, Meister M (2016) A neuronal circuit for colour vision based on rod-cone opponency. Nature 532:236–239.

Kelber A, Vorobyev M, Osorio D (2003) Animal colour vision--behavioural tests and physiological concepts. Biol Rev Camb Philos Soc 78:81–118.

Khabou H, Desrosiers M, Winckler C, Fouquet S, Auregan G, Bemelmans A-P, Sahel JA, Dalkara D (2016) Insight into the mechanisms of enhanced retinal transduction by the engineered AAV2 capsid variant -7m8. Biotechnol Bioeng 113:2712–2724.

Kim JS, Greene MJ, Zlateski A, Lee K, Richardson M, Turaga SC, Purcaro M, Balkam M, Robinson A, Behabadi BF, Campos M, Denk W, Seung HS, EyeWirers (2014) Space-time wiring specificity supports direction selectivity in the retina. Nature 509:331–336.

Lind O, Mitkus M, Olsson P, Kelber A (2013) Ultraviolet sensitivity and colour vision in raptor foraging. J Exp Biol 216:1819–1826.

Marshak DW, Mills SL (2014) Short-wavelength cone-opponent retinal ganglion cells in mammals. Vis Neurosci 31:165–175.

Martin PR, Lee BB, White AJ, Solomon SG, Rüttiger L (2001) Chromatic sensitivity of ganglion cells in the peripheral primate retina. Nature 410:933–936.

Marvin JS, Borghuis BG, Tian L, Cichon J, Harnett MT, Akerboom J, Gordus A, Renninger SL, Chen TW, Bargmann CI, Orger MB, Schreiter ER, Demb JB, Gan W-B, Hires SA, Looger LL (2013) An optimized fluorescent probe for visualizing glutamate neurotransmission. Nat Methods 10:162–170.

Maximov VV (2000) Environmental factors which may have led to the appearance of colour vision. Philos Trans R Soc Lond B Biol Sci 355:1239–1242.

Mills SL, Tian LM, Hoshi H, Whitaker CM, Massey SC (2014) Three distinct blue-green color pathways in a mammalian retina. J Neurosci 34:1760–1768.

Murphy-Baum BL, Taylor WR (2015) The synaptic and morphological basis of orientation selectivity in a polyaxonal amacrine cell of the rabbit retina. J Neurosci 35:13336–13350.

Neitz J, Neitz M (2011) The genetics of normal and defective color vision. Vision Res 51:633–651.

Olveczky BP, Baccus SA, Meister M (2003) Segregation of object and background motion in the retina. Nature 423:401–408.

Packer OS, Verweij J, Li PH, Schnapf JL, Dacey DM (2010) Blue-yellow opponency in primate S cone photoreceptors. J Neurosci 30:568–572.

Peichl L (2005) Diversity of mammalian photoreceptor properties: adaptations to habitat and lifestyle? Anat Rec A Discov Mol Cell Evol Biol 287:1001–1012.

Peichl L, González-Soriano J (1994) Morphological types of horizontal cell in rodent retinae: a comparison of rat, mouse, gerbil, and guinea pig. Vis Neurosci 11:501–517.

Peichl L, Künzle H, Vogel P (2000) Photoreceptor types and distributions in the retinae of insectivores. Vis Neurosci 17:937–948.

Peichl L, Sandmann D, Boycott BB (1998) Comparative Anatomy and Function of Mammalian Horizontal Cells. In: Development and organization of the retina: From molecules to function (Chalupa LM, Finlay BL, eds), pp 147–172. Boston, MA: Springer US.

Pfeiffer K, Homberg U (2007) Coding of azimuthal directions via time-compensated combination of celestial compass cues. Curr Biol 17:960–965.

Potier S, Mitkus M, Kelber A (2018) High resolution of colour vision, but low contrast sensitivity in a diurnal raptor. Proc R Soc B 285:20181036.

Puller C, Haverkamp S (2011) Bipolar cell pathways for color vision in non-primate dichromats. Vis Neurosci 28:51–60.

Rabl K, Cadetti L, Thoreson WB (2005) Kinetics of exocytosis is faster in cones than in rods. J Neurosci 25:4633–4640.

Rodieck RW (1991) The density recovery profile: a method for the analysis of points in the plane applicable to retinal studies. Vis Neurosci 6:95–111.

Röhlich P, van Veen T, Szél A (1994) Two different visual pigments in one retinal cone cell. Neuron 13:1159–1166.

Román Rosón M, Bauer Y, Kotkat AH, Berens P, Euler T, Busse L (2019) Mouse dLGN receives functional input from a diverse population of retinal ganglion cells with limited

convergence. Neuron 102:462–476.e8.

Rossi J, Balthasar N, Olson D, Scott M, Berglund E, Lee CE, Choi MJ, Lauzon D, Lowell BB, Elmquist JK (2011) Melanocortin-4 receptors expressed by cholinergic neurons regulate energy balance and glucose homeostasis. Cell Metab 13:195–204.

Schlamp CL, Montgomery AD, Mac Nair CE, Schuart C, Willmer DJ, Nickells RW (2013) Evaluation of the percentage of ganglion cells in the ganglion cell layer of the rodent retina. Mol Vis 19:1387–1396.

Shekhar K, Lapan SW, Whitney IE, Tran NM, Macosko EZ, Kowalczyk M, Adiconis X, Levin JZ, Nemesh J, Goldman M, McCarroll SA, Cepko CL, Regev A, Sanes JR (2016) Comprehensive classification of retinal bipolar neurons by single-cell transcriptomics. Cell 166:1308–1323.e30.

Sher A, DeVries SH (2012) A non-canonical pathway for mammalian blue-green color vision. Nat Neurosci 15:952–953.

Stabio ME, Sabbah S, Quattrochi LE, Ilardi MC, Fogerson PM, Leyrer ML, Kim MT, Kim I, Schiel M, Renna JM, Briggman KL, Berson DM (2018) The M5 cell: A color-opponent intrinsically photosensitive retinal ganglion cell. Neuron 97:150–163.e4.

Ströh S, Sonntag S, Janssen-Bienhold U, Schultz K, Cimiotti K, Weiler R, Willecke K, Dedek K (2013) Cell-specific cre recombinase expression allows selective ablation of glutamate receptors from mouse horizontal cells. PLoS One 8:e83076.

Szél A, Röhlich P, Caffé AR, Juliusson B, Aguirre G v., Van Veen T (1992) Unique topographic separation of two spectral classes of cones in the mouse retina. J Comp Neurol 325:327–342.

Szikra T, Trenholm S, Drinnenberg A, Jüttner J, Raics Z, Farrow K, Biel M, Awatramani G, Clark DA, Sahel J-A, da Silveira RA, Roska B (2014) Rods in daylight act as relay cells for cone-driven horizontal cell-mediated surround inhibition. Nat Neurosci 17:1728–1735.

Thoreson WB, Dacey DM (2019) Diverse cell types, circuits, and mechanisms for color vision in the vertebrate retina. Physiol Rev 99:1527–1573.

Tikidji-Hamburyan A, Reinhard K, Storchi R, Dietter J, Seitter H, Davis KE, Idrees S, Mutter M, Walmsley L, Bedford RA, Ueffing M, Ala-Laurila P, Brown TM, Lucas RJ, Münch TA (2017) Rods progressively escape saturation to drive visual responses in daylight conditions. Nat Commun 8:1813.

Trümpler J, Dedek K, Schubert T, de Sevilla Müller LP, Seeliger M, Humphries P, Biel M, Weiler R (2008) Rod and cone contributions to horizontal cell light responses in the mouse retina. J Neurosci 28:6818–6825.

Verweij J, Kamermans M, Spekreijse H (1996) Horizontal cells feed back to cones by shifting the cone calcium-current activation range. Vision Res 36:3943–3953.

Wässle H, Riemann HJ (1978) The mosaic of nerve cells in the mammalian retina. Proc R Soc Lond B Biol Sci 200:441–461.

Wei T, Schubert T, Paquet-Durand F, Tanimoto N, Chang L, Koeppen K, Ott T, Griesbeck O, Seeliger MW, Euler T, Wissinger B (2012) Light-driven calcium signals in mouse cone photoreceptors. J Neurosci 32:6981–6994.

Welch JF (1953) Formation of urinating “posts” by house mice (Mus) held under restricted conditions. J Mammal 34:502–503.

Wood SN (2006) Generalized additive models: an introduction with R. Chapman and Hall/CRC Texts in Statistical Science.

Wool LE, Packer OS, Zaidi Q, Dacey DM (2019) Connectomic identification and three-dimensional color tuning of S-OFF midget ganglion cells in the primate retina. J Neurosci Available at: http://dx.doi.org/10.1523/JNEUROSCI.0778-19.2019.

Yin L, Smith RG, Sterling P, Brainard DH (2009) Physiology and morphology of color-opponent ganglion cells in a retina expressing a dual gradient of S and M opsins. J Neurosci 29:2706–2724.

Zhao Z, Klindt D, Chagas AM, Szatko KP, Rogerson LE, Protti D, Behrens C, Dalkara D, Schubert T, Bethge M, Franke K, Berens P, Ecker AS, Euler T (2019) The temporal structure of the inner retina at a single glance. bioRxiv:743047 Available at: https://www.biorxiv.org/content/10.1101/743047v1.

ACKNOWLEDGMENTS

We thank G. Eske for excellent technical support, S. Haverkamp and T. Baden for feedback and discussions and J. Marvin and L. Looger for providing the viral vector (pAAV.hSyn.iGluSnFR). This work was supported by the German Federal Ministry of Education and Research (BMBF: FKZ: 01GQ1002 and 01GQ1601), the German Research Foundation (DFG: BE5601/4; SFB1233, project number 276693517; EXC 2064, project number 390727645; SCU 2243/3-1) and the Max Planck Society (MPG: M.FE.A.KYBE0004).

AUTHOR CONTRIBUTIONS

K.F. designed the study with input from T.E.; D.D. produced the iGluSnFR virus; K.F. performed viral injections; M.K. performed OPL recordings with help from K.F. and T.S.; K.F. performed IPL recordings; K.S. performed GCL recordings with help from K.F.; Y.R. performed electrical recordings; M.K., K.F. and K.S. performed pre-processing; K.F. analyzed the data with input from T.E. and P.B.; K.F. prepared the figures with help from K.S. and M.K.; M.K., K.F., K.S., P.B. and T.E. wrote the manuscript.